



**T.C.
ISTANBUL UNIVERSITY
INSTITUTE OF SCIENCE**



MASTER THESIS

**INVESTIGATION OF LONG-TERM CHANGES AND
VARIATIONS OF THE SYMBIOTIC STAR R AQUARI AND IT'S
JETS**

Havva BOSTAN

Astronomy and Astrophysics

SUPERVISOR


Prof. Dr. Şölen BALMAN

June, 2024

ISTANBUL

This study was accepted as a Master Thesis in Department of Astronomy and Space Sciences
by the following jury on 11.06.2024

Jury of the Thesis



Prof. Dr. Şölen BALMAN
(Supervisor)
Istanbul University
Faculty of Science

Prof. Dr. Ahmet Talat SAYGAÇ
Istanbul University
Faculty of Science

Assoc. Prof. Murat HÜDAVERDİ
Yıldız Technical University
Faculty Of Arts & Science



- **Declaration of Plagiarism**

According to articles 9/2 and 22/2 of the Regulation on Graduate Education and Training published in the Official newspaper on 20.04.2016, this graduate thesis has been reported according to the criteria determined by the Graduate School of Natural and Applied Sciences by using the plagiarism software program subscribed by Istanbul University.

- **Project Support**

This study was supported by the project numbered 40017 conducted by Prof. Dr. Şölen Balman within the Scientific Research Projects Directorate of Istanbul University.

- **Imprint Information of Publications Produced from Thesis**

[]

PREFACE

Firstly, I am immensely thankful to my esteemed supervisor, Prof. Dr. Şölen BALMAN, for her invaluable contributions in shaping my path throughout this study. Her perseverance and profound knowledge have been instrumental in guiding me since the beginning of this study. I am very grateful to have the opportunity to be supervised by her.

I would like to express my grace to my family for their intense support in this ongoing process. I would also like to thank my dearest friend Burak Cem COŞKUN, who has been an ally in all circumstances and has made a significant impact on my personal growth and worldview.

Lastly, I would like to express my gratitude to the lecturers in the Department of Astronomy and Space Science for imparting their knowledge and expertise during my courses, and to my dear friends for their support and companionship.

I dedicate this work to all those who, throughout human history, have attempted to comprehend the universe and contribute to its advancement.

June, 2024

Havva BOSTAN

CONTENTS

	Page No
PREFACE	iv
CONTENTS	vi
LIST OF FIGURES	ix
LIST OF TABLES	x
LIST OF SYMBOLS AND ABBREVIATIONS	xii
ÖZET	xiii
ABSTRACT	xiv
1. INTRODUCTION	1
1.1. A CONCISE HISTORICAL OVERVIEW	2
2. GENERAL PARTS	3
2.1. WHITE DWARF SYMBIOTICS	3
2.2. WIND ACCRETION IN SYMBIOTIC SYSTEMS	4
2.3. OUTBURSTS IN SYMBIOTIC SYSTEMS	9
2.4. JETS IN SYMBIOTIC SYSTEMS	10
2.5. SHOCKS IN SYMBIOTIC SYSTEMS	12
2.6. SYMBIOTIC STARS IN X-RAYS	14
2.7. A LOOK INTO A GLORIOUS SYSTEM: R AQR	17
3. MATERIAL AND METHODS	23
3.1. X-RAY OBSERVATIONS	23
3.1.1. Chandra X-Ray Observatory	23
3.1.2. Observations of R Aqr	23
3.2. IMAGE PROCESSING	25
3.2.1. X-ray Emission Morphology	25
3.2.2. Line Energy Images	31
3.3. SPECTRAL ANALYSIS	32
3.3.1. Spectra of 1".5 Region Around the Central Source	33
3.3.2. Spectra of 1".5 Region Around the Off-center	36
3.3.3. Spectrum of 8" Region Towards to NE Direction	43

4. DISCUSSIONS AND CONCLUSIONS	45
4.1. X-RAY MORPHOLOGY OF R AQR	45
4.2. X-RAY SPECTRA OF R AQR	46
4.2.1. Central Region Spectra Using Model1	46
4.2.2. Elaboration on the Central Region Spectra Using Model2	48
4.2.3. On the Interpretation of the Off-center Region Spectra	50
4.2.4. NE Region Spectrum	51
4.3. COMPARISON WITH PREVIOUS CHANDRA OBSERVATIONS	51
4.4. CONCLUSIONS	52
REFERENCES	56
APPENDIX	60
1. 2005 Chandra Data	60
CURRICULUM VITAE	63

LIST OF FIGURES

	Page No
Figure 1.1: Schematic view of a symbiotic system consisting a hot white dwarf and cool giant star adopted from Figure 1. of J. Merc (2022).	3
Figure 2.1: Schematic view of Roche-lobe equipotential surfaces of components, mass transfer at L1 point from primary to secondary, and an accretion disk formation around the WD/secondary adopted from Figure 8.1 of R. L. Coto (2015)	4
Figure 2.2: A detailed schematic view of the chemical structure of the core, atmospheric layers, and environment of an AGB star, including its radius and the processes occurring in these regions adopted from Figure 1. of S. Höfner & H. Olofsson (2018)	7
Figure 2.3: Schematic view of WRLOF in binary systems, wind acceleration zone, and formation of an accretion disk around the WD adopted from Figure 3.8 of X. Chen et al. (2023).....	8
Figure 2.4: Schematic view of L1 point and the wind acceleration zone of the orbit in binary systems adopted from Figure 1. of C. Abate et al. (2013). R_d represent the wind acceleration radius, $R_{L,1}$ represent the Roche-lobe radius of the giant, R_* represent the radius of the primary star, and L_1 is the Lagrange1 point of the orbit. The radii are not to scale.	8
Figure 2.5: Schematic representation of symbiotic colliding winds. The open and filled circles indicate the WD and giant components of the system, respectively. The surrounding medium (I) is constituted by mass lost by the cool component before the initiation of the hot component wind (II). Cwb represent the binary colliding winds and Cwc is concentric colliding winds. Figure is adopted from Figure 1. of Kenny et. al. 2005.	12
Figure 2.6: A schematic view of the structure around a symbiotic system, with the binary and accretion disk at the center adopted from Figure 7. of J. Toala (2024). The system without extended emission is on the left side of the vertical dashed line, while the system displaying bipolar ejections or jets is on the right side. Line of sights are indicated by the black arrows and labels ($\alpha - \beta - \delta - \beta/\delta$). Sketch is not to scale.....	16
Figure 2.7: HST image of R Aqr with a scale of $\sim 45'' \times 45''$ taken with $H\alpha$ filter on October 18,2014 adopted from Figure 1. of Melnikov et. al. 2018.....	19
Figure 2.8: Narrow-band $H\alpha$ image of R Aqr from VLT/SPHERE-ZIMPOL with a scale of $70'' \times 70''$. $3''.5 \times 3''.5$ central area is indicated with the circle and the central binary is marked with two dots. Image taken on October 2014 and adopted from Figure 1. of Schmid et. al. 2017.	20

Figure 2.9: Left: Broadband H α image of R Aqr taken on October 11, 2014, with VLT/SPHERE-ZIMPOL telescope. Right: The first resolved image of the R Aqr was obtained when the Mira was at its minimum brightness on October 11, 2014, using the Narrow H α filter on the VLT/SPHERE-ZIMPOL telescope. Images adopted from Figure 4a-4b of Schmid et al. 2017.	22
Figure 3.1: Schematic view of <i>Chandra</i> X-ray Telescope and its instruments. Image credit NASA/CXC.	24
Figure 3.2: <i>Chandra</i> images of R Aqr in the 0.3 - 10.0 keV with the resolution of 0.5" pixel size. Gaussian smoothing $\sigma = 2$ pix was used for each image. The top left shows 2017 data the top right 2020 data, the bottom left 2021 data, and the bottom right 2022 data. The location of the central source is indicated by the orange cross for each image.	26
Figure 3.3: Images of R Aqr in the 0.3-1.5 keV range with 0".25 pixel size. Colormap and scale parameters are identical in all the images. Gaussian smoothing $\sigma = 2$ pix was used for each image. The corresponding year is indicated at the top left of each image. The red cross sign indicates the location of the central binary system.	28
Figure 3.4: Images of R Aqr in the 2.0-5.0 keV range with 0".25 pixel size for each year. Gaussian smoothing $\sigma = 2$ pix was used for each image. The corresponding year is indicated at the top left hand side of each image. The location of the central source is indicated by a red cross sign.	29
Figure 3.5: Images of R Aqr in the 5.0 - 8.0 keV range with a resolution of 0.25" for each year. Gaussian smoothing $\sigma = 2$ pix was used for each image. The corresponding year is indicated at the top left hand side of each image. The location of the central source is indicated by a red cross sign.	30
Figure 3.6: Narrow-band images of R Aqr in the 0.3-0.7 keV range for 2017 and 2020 data, respectively. Gaussian smoothing $\sigma = 2$ pix was used for both images. The location of the central source is indicated by a red cross sign.	31
Figure 3.7: The circular regions with a radius of 1".5 from which the central source region spectra were taken are indicated by the red circles. The top left shows 2017 data the top right 2020 data, the bottom left 2021 data, and the bottom right is the 2022 data.	34
Figure 3.8: X-ray spectra and best-fit models of the 1".5 region around R Aqr using the Model1 in 2017, 2020 (top panel, left to right), 2021, 2022 (bottom panel, left to right). Data are shown in pink and fits are shown in green. The blue dotted lines show, the soft component and the orange dotted lines show the hard component. The Gauss line is shown in red dashed lines. The second panel of each spectrum shows the residuals of the fits in standard deviations.	37
Figure 3.9: X-ray spectra and best-fit models of the 1".5 region around R Aqr using Model2 in 2017, 2020 (top panel, left to right), and 2021, 2022 (bottom panel, left to right). Data are shown in pink and fits are shown in black. The soft component is in blue, and the first emission component of the hard X-ray is in orange second is in vibrant pink. The Gauss line is shown in red dashed lines. The second panel of each spectrum shows the residuals of the fits in standard deviations.	39

Figure 3.10: The 1.5" circular regions from which the off-center spectra were chosen are indicated by the purple circles. The top left shows 2017 data the top right 2020 data, the bottom left 2021 data, and the bottom right is the 2022 data.	41
Figure 3.11: X-ray spectra of 1".5 region towards the SW direction of R Aqr in the years 2017, 2020 (top panel, left to right), and 2021, 2022(bottom panel, left to right). Data are shown in pink and fits are shown in green. The second panel of each spectrum shows the residuals of the fits in standard deviations.	42
Figure 3.12: The yellow circle shows the 8" radius region from which the NE spectrum of 2017 was extracted.	43
Figure 3.13: X-ray spectrum of 8" region in the NE direction of R Aqr in the year 2017. Data are shown in blue and fits are shown in black. The lower panel shows the residuals of the fit in standard deviations.	44
Figure 1.1: Chandra X-ray spectrum and the best fit model of 1".5 region around R Aqr using data obtained in 2005. Data are shown in black and fit is in green. The second panel of the spectrum shows the residuals of the fit in standard deviations.	60

LIST OF TABLES

	Page No
Table 3.1: The data referenced in this study.....	25
Table 3.2: Spectral Fit Parameters in the 1".5 central source region. Model1 is used: $tbabs \times (pcfabs \times nei + (zxipcf \times (nei + gauss)))$	38
Table 3.3: Spectral Fit Parameters in the 1".5 central source region. Model2 is used: $tbabs \times (pcfabs \times nei + zxipcf \times (bremss + nei + gauss))$	40
Table 3.4: Spectral Fit Parameters in the 1".5 off-center region. Model is used: $tbabs \times (pcfabs \times nei)$	41
Table 3.5: Spectral Fit Parameters of the 8" radius region in the NE direction. Model is used: $tbabs \times (pcfabs \times nei)$	44
Table 1.1: Spectral Parameters of the central region with a radius of 1".5 radius for the 2005 epoch. Model is used: $tbabs \times ((pcfabs \times nei) + zxipcf \times (nei + gauss))$	61

List of Symbols and Abbreviations

Symbol	Definition
A	: Angstrom
"	: Arc second
cm	: Centimeter
k	: Boltzmann constant
K	: Kelvin
keV	: Kilo electron Volt
L	: Luminosity
m_H	: Mass of hydrogen atom
μ	: mean molecular weight
N_H	: Neutral hydrogen column density
s	: Second
M_\odot	: Solar Mass
R_\odot	: Solar Radius

Abbreviations	Definition
<i>AGNs</i>	: Active Galactic Nucleus
<i>AU</i>	: Astronomical Unit
<i>BL</i>	: Boundary Layer
<i>CIAO</i>	: Chandra Interactive Analysis of Observations
<i>CVs</i>	: Cataclysmic Variables
<i>CXO</i>	: Chandra X-ray Observatory
<i>EXOSAT</i>	: The European X-ray Observatory Satellite
<i>FORCAST</i>	: Faint Object infraRed Camera for the SOFIA Telescope
<i>HST</i>	: Hubble Space Telescope
<i>IEU</i>	: International Ultraviolet Explorer
<i>nei</i>	: Non-equilibrium ionization collisional plasma model
<i>R Aqr</i>	: R Aquarii
<i>RG</i>	: Red Giant

<i>ROSAT</i>	: The Roentgen Satellite
<i>RLOF</i>	: Roche-lobe Overflow
<i>WD</i>	: White Dwarf
<i>SPHERE</i>	: Spectro-Polarimetric High-contrast Exoplanet Research Instrument
<i>SOFIA</i>	: Stratospheric Observatory for Infrared Astronomy
<i>SS/SySts/SySt</i>	: Symbiotic Stars
<i>SyXBs</i>	: Symbiotic X-ray Binaries
<i>tbabs</i>	: The Tuebingen-Boulder ISM absorption model
<i>VLT</i>	: Very Large Telescope
<i>WD</i>	: White Dwarf
<i>WRLOF</i>	: Wind Roche-lobe Overflow
<i>XRBs</i>	: X-Ray Binaries
<i>XSPEC</i>	: X-ray Spectral-Fitting Package
<i>YSO</i>	: Young Stellar Object
<i>ZIMPOL</i>	: Zurich Imaging Polarimeter

ÖZET

YÜKSEK LİSANS TEZİ

SİMBİYOTİK YILDIZ R AQUARII VE JETLERİNİN UZUN DÖNEMLİ DEĞİŞİM VE VARYASYONLARININ İNCELENMESİ

Havva BOSTAN

İstanbul Üniversitesi

Fen Bilimleri Enstitüsü

Astronomi ve Astrofizik

Danışman: Prof. Dr. Şölen BALMAN

Simbiyotik yıldızlar tipik olarak bir beyaz cüce ve bir Mira değişeni ya da bir dev yıldızdan oluşan ikili sistemlerdir. R Aqr, farklı dalga boylarında incelenmiş olan bir Mira ve bir beyaz cüceden oluşan iyi bilinen bir simbiyotik sistemdir. Bu sistem bazı dönemlerde iki kutuplu jet akışlarına sahiptir. Bu tez, X-ışınlarında jetlerin yapısı ve sistemin kendisi üzerine kapsamlı bir çalışma sunmaktadır. Beş yılı kapsayan Chandra arşiv verileri, jetleri ve merkezi kaynağı hem uzamsal hem de spektral özellikler açısından araştırmak için kullanıldı. Spektral analizde, merkezi kaynağı ve çevresini anlamak için iki farklı bileşik model kullanıldı. Sistemi daha iyi anlamak için 2000, 2003 ve 2005 yıllarında alınan veriler kullanılarak önceki Chandra analizleri ile karşılaştırmalar yapıldı. Bu, sistemin geçmişinin yaklaşık yirmi yılını kapsamaktadır. Jetlerin X-ışını emisyonu ağırlıklı olarak 1 keV'nin altındaki yumuşak X-ışınlarında gözlenmekte ve kısa zaman ölçeklerinde $\approx 2 - 3$ yıl X-ışını emisyonlarında azalma gibi değişimler sergilemektedir. Zaman içinde, sistem morfolojisinde $\approx 6''$ den $\approx 3''$ 'ne kadar belirgin değişiklikler tespit edilmiştir. Sonuç olarak, bu çalışma X-ışınlarında bu dinamik sistemin yapısının ve davranışının daha ayrıntılı bir şekilde anlaşılmasına katkıda bulunmuştur.

Haziran 2024, 77 sayfa.

Anahtar kelimeler: Simbiyotik yıldızlar, R Aquarii, X-ray, Chandra

ABSTRACT

M.Sc. THESIS

INVESTIGATION OF LONG-TERM CHANGES AND VARIATIONS OF THE SYMBIOTIC STAR R AQUARII AND IT'S JETS

Havva BOSTAN

İstanbul University

Institute of Sciences

Astronomy and Astrophysics

Supervisor: Prof. Dr. Şölen BALMAN

Symbiotic stars are binary systems that typically comprise a white dwarf and a Mira-type variable or a giant star. R Aquarii is a well-known symbiotic system, consisting of a Mira and a white dwarf, which has been studied over the entire electromagnetic spectrum. This system has bipolar jet outflows in some periods. This thesis presents a comprehensive study of the structure of the jets and the system itself in X-rays. Chandra archival data, covering five years, was used to investigate jets and the central source in terms of both spatial and spectral characteristics. In spectral analysis, two different composite models were used to understand the central source and its surroundings. To gain a deeper understanding of the system, comparisons were made with previous Chandra analyses, using data taken in 2000, 2003, and 2005. This encompasses approximately two decades of the system's history. The X-ray emission of jets is predominantly observed in soft X-rays below 1 keV and exhibits variations on short timescales $\approx 2 - 3$ years, such as a decrease in X-ray emission. Over time, distinct changes in the system morphology from $\approx 6''$ to $3''$ were identified. In conclusion, this study has contributed to a more detailed understanding of the structure and the behavior of this dynamical system in the X-rays.

June 2024, 77 pages.

Keywords: Symbiotic stars, R Aquarii, X-ray, Chandra

1. INTRODUCTION

Stars are the most exotic part of our known universe. Like all matter in the universe, during its long life, a star undergoes changes in its structure along with the changes in the nuclear reactions in its nucleus. The mass of a star is the most significant factor in determining these changes. During this time, it usually has gravitationally bound companion orbiting around a common center of mass, and its companion also has an effect on this change. This motion of the two objects around the common center of mass is known as a binary system, and it plays a crucial role in the stars' evolution.

Binary systems constitute the majority of stellar systems in the Universe. Symbiotic stars (SySts) are a type of binary system typically classified as a subclass of accreting white dwarf binaries (AWDs). A typical symbiotic star system consists of a hot compact object (generally a WD) and an M-type red giant star or Mira-type star. A white dwarf is the last stage of stars with an initial mass of less than $8 M_{\odot}$. At this stage, the star is no longer in thermal equilibrium and is supported by degenerate electron pressure. Giant stars have extremely large radii, several hundred solar radii, which are in the post main sequence evolution from low to intermediate-mass stars between $0.5 - 8.0 M_{\odot}$.

SySts are categorized into two types based on the type of compact object they contain: white dwarf symbiotics (WD Symbiotics) and symbiotic X-ray binaries (SyXBs). Symbiotic X-ray binaries have neutron stars as compact objects, while white dwarf symbiotics have white dwarfs. The number of SyXBs known to date is very small compared to the number of WD symbiotics. Only five systems have been confirmed as belonging to this class. In this thesis, we only focus on the white dwarf symbiotics and specially the R Aqr system in X-ray wavelengths.

Symbiotic stars play an important role in the study of various topics such as wind accretion, jet structures, dust formation, and accretion discs due to their long periods and wide binary separation. Additionally, as the hot component of white dwarf symbiotics is the white dwarf and there is mass accretion; it is widely believed that WD symbiotics are progenitors of supernovae Type Ia.

1.1. A CONCISE HISTORICAL OVERVIEW

In 1912, Williamina Fleming published a collaborative work with Edward Pickering on the spectra of variable stars in the annals of the Harvard College Observatory. The study was titled 'stars having peculiar spectra' and included a few stars that are now known to be symbiotic stars.

With the expansion of these studies, they made new additions to the stars having peculiar spectra in 1914 and separated the double stars, which they called having a combined spectrum, as a separate type. In 1932 Paul W. Merrill & Milton L. Humason published three new stellar composite spectra which have high excitation emission lines with ionized Helium at 4686Å (He II 4686) and low excitation absorption lines with titanium oxide (TiO).

In 1958, Paul W. Merrill coined the term symbiotic stars. The reason that he chose this word is because of the combination of H I, He II emission lines, and TiO absorption lines of low-temperature star observed in the optical spectra of such stars.

At the beginning, there were lots of questions about these odd symbiotic stars. From the spectra, it was clear that these systems had M-type giant stars, but the strangeness could have been due to the change of the M-type star itself, whether it had a second component, or whether the star was surrounded by a planetary nebula. In 1981, astronomers confirmed that symbiotic systems were binaries by observing the Z Andromedae system with the International Ultraviolet Explorer (IEU) and examining its ultraviolet spectrum.

In 1984, the general view on the content of a symbiotic system was as follows 1) a late type or bright giant 2) a hot component (white dwarf/main sequence star) surrounded by an accretion disk around the giant or compact star such as the central star of planetary nebula 3) surrounding nebula ionized by the hot component.

Today's understanding of a symbiotic star system is that it comprises a red giant and a hot component, mostly a WD, and the surrounding gaseous nebula. In the system's spectra, we can observe absorption features of the giant, such as TiO bands or Ca I - Ca II absorption lines, along with emission lines of H I and He II. Figure 1.1 illustrates the generic view of a symbiotic system.

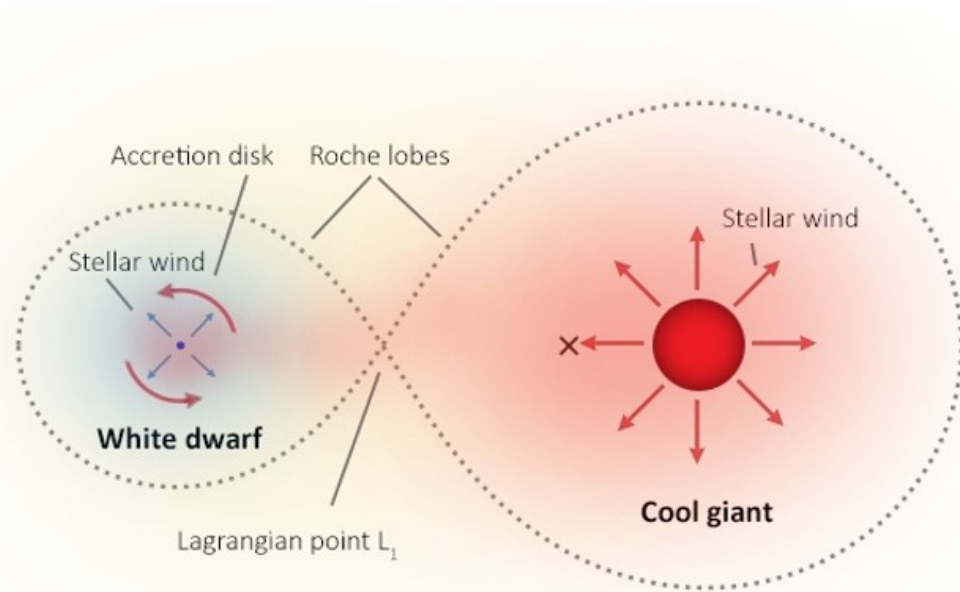


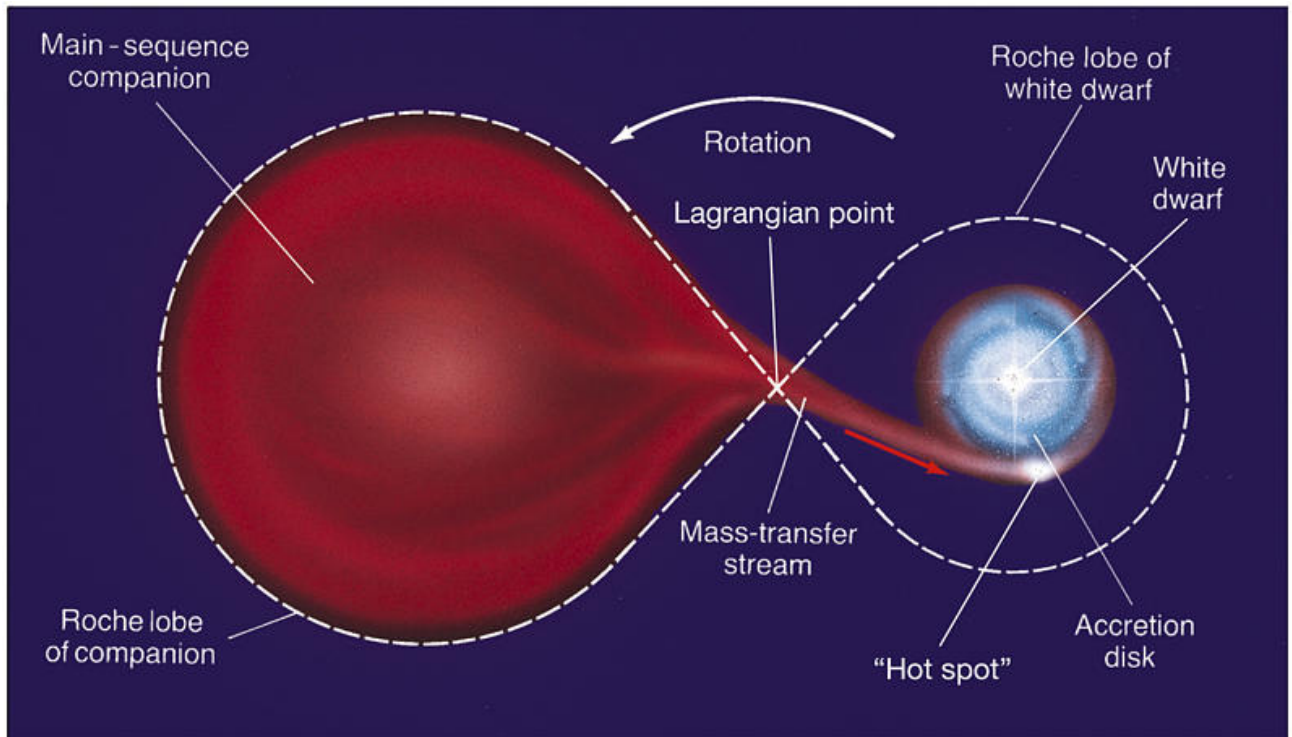
Figure 1.1: Schematic view of a symbiotic system consisting of a hot white dwarf and cool giant star adopted from Figure 1. of J. Merc (2022).

2. GENERAL PARTS

2.1. WHITE DWARF SYMBIOTICS

Although symbiotic stars were initially observed in the optical band, subsequent observations have been conducted across various wavelengths. By observing at different wavelengths, the systems were understood better and it turns out that there are different types of WD Symbiotics.

According to their infrared spectra, WD Symbiotics differ from each other in the type of giant they host. They are categorized as Stellar-type (S-type) and Dusty-type (D-type) symbiotics. S-type symbiotics contain red giants and D-type symbiotics contain Mira-type giants. The majority of WD Symbiotics belong to the S-type. There are also S+IR and D'-type symbiotic systems. D'-type systems differ from D-type systems as they contain G/K type giants and two peaks between 2-10 μm (longer wavelengths than D-type). S+IR-type symbiotics show peaks in their IR spectrum at longer wavelengths compared to S-type symbiotics. This



Copyright © 2005 Pearson Prentice Hall, Inc.

Figure 2.1: Schematic view of Roche-lobe equipotential surfaces of components, mass transfer at L1 point from primary to secondary, and an accretion disk formation around the WD/secondary adopted from Figure 8.1 of R. L. Coto (2015)

indicates that S+IR-type symbiotics have lower-temperature giant components.

Differences in characteristics such as binary separation, the density of the nebula surrounding the system and the orbital period arise from the different types of donor stars in S- and D-type systems. D-type symbiotics have relatively long orbital periods, spanning tens of years, while S-type symbiotics have 200-2000 days orbital periods. D-type systems have wider binary separation, typically around 20 AU, whereas S-type systems are much closer, with a separation of 1-3 AU. The S-type nebulae are denser and more compact, with a density of $10^8 - 10^9 \text{ cm}^{-3}$, while the D-type nebulae are thinner and more extended, with a density of 10^5 cm^{-3} .

2.2. WIND ACCRETION IN SYMBIOTIC SYSTEMS

In a binary system, mass transfer occurs from one component to the other in the course of the evolution of the system which involves an increase of radius of the evolving stars and mass ejection. The type of components and the binary separation are important factors in

mass transfer.

The Roche geometry of the system is a crucial indicator for mass transfer processes. Roche geometry is based on the concept of Roche equipotential surfaces which is widest limit of the system's orbit where the atmospheres of the components can expand. According to Roche geometry of a binary system, there are five points of the system orbit that the gravitational pulls of the components are equal. These points are called Lagrange points, L1-L2-L3-L4-L5. Lagrange points are equilibrium points, while L1, L2, and L3 are unstable L4 and L5 are stable points. Mass transfer in a binary system occurs at the inner Lagrangian point (L1).

Mass transfer in binary systems occurs either at the Lagrange1 (L1) point, located between the components of the system when the primary star fills its Roche equipotential surface and matter is accreted to the secondary, called the Roche-lobe overflow (RLOF), or when material ejected by the primary's stellar winds is captured by the gravitational pull of the secondary.

Unlike cataclysmic variables (CV), which are a type of binary system consisting of a white dwarf and a late-type main sequence star, the binary separation of the SySts is comparatively larger, in the order of astronomical units. In CV-like systems, i.e. the system's primary star fills its Roche-lobe, the mass transfer occurs through RLOF processes, while in symbiotic stars, the wind plays a significant role in mass transfer. Figure 2.1 shows a schematic view of a process called Roche-lobe overflow (RLOF), with an example, CV system, where the mass is transferred from the L1 point of the primary star as the secondary star fills its Roche-lobe and an accretion disk is formed around the secondary.

Bondi-Hoyle-Lyttleton (BHL) wind accretion is a process where spherically symmetric supersonic motion is directed onto a central point mass. It was previously believed to occur in wind-driven systems such as symbiotic stars. However, in 2007, S. Mohamed & Ph. Podsiadlowski proposed a new mass transfer process, similar to Roche-lobe overflow, but for wide binaries. The reason for this new process was that the required mass accretion rate in BHL accretion was found to be lower than typically observed in Asymtotic Giant Branch (AGB) stars. However, a study conducted in 2010 by Sokoloski and Bildsten on the Mira AB system found that both gravitational focusing and Wind Roche-lobe overflow did not improve the efficiency of accretion onto the WD in this system.

In many symbiotic systems, while the secondary is a hot (50000 - 200000 K) WD, the primary star is a cool (3000 - 4000 K) giant star that has not filled its Roche lobe and is losing $10^{-7} - 10^{-5} M_{\odot} \text{ yr}^{-1}$ mass with winds of up to $5\text{-}30 \text{ km s}^{-1}$. In this paper the secondary term is used for the WD of the system and the primary term is used for the donor giant star. Giant stars are a major contributor to dust production in the universe. They produce gas and dust through convective motions that carry material into their outer atmospheres.

The temperature of the dust grains is defined as

$$T_d(r) \approx T_* \left(\frac{2r}{R_*} \right)^{-\frac{2}{4+p}} \quad (2.1)$$

where T_d is the temperature of the dust grains, R_* is the radius of the giant, T_* is the temperature of the giant, and p is the material-dependent constant.

Dust grains play an important role in the mass accretion processes of a system with wind accretion in progress. The primary star's wind is accelerated due to radiation pressure on the dust grains. The wind acceleration zone is the area where wind speeds exceed the escape velocity. Figure 2.2 shows the core and outer atmosphere layers with the chemical composition of an AGB star and a detailed representation of the processes that take place in these layers.

In symbiotic stars, mass transfer occurs via wind accretion or wind-RLOF, instead of classical Roche-lobe overflow (RLOF). Wind-RLOF occurs when the wind from the giant star accumulates and transfers mass towards the secondary star, typically from the L1 point in the system. Figure 2.3 provides a schematic representation of a binary system undergoing mass transfer via wind Roche-lobe overflow. As a result of this wind accretion mechanism, an accretion disk can form around the white dwarf, enhancing the complexity and dynamics of the system.

The wind-RLOF mechanism occurs in two distinct situations. The first scenario occurs when the wind speed of the giant stars is less than the escape velocity of the Roche-lobe surface, $v_{wind}(R_L) < v_{esc}(R_L)$. This is associated with conditions where the wind outflow of the giant is slow, approximately 4 km s^{-1} . The second scenario occurs when the wind acceleration

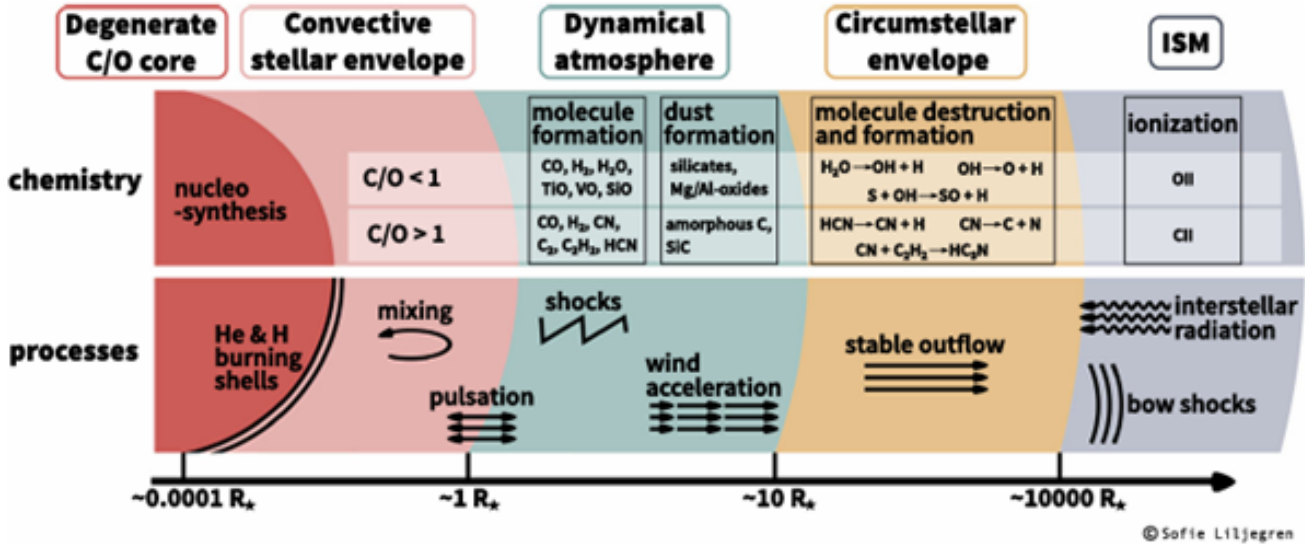


Figure 2.2: A detailed schematic view of the chemical structure of the core, atmospheric layers, and environment of an AGB star, including its radius and the processes occurring in these regions adopted from Figure 1. of S. Höfner & H. Olofsson (2018)

zone, also known as the dust formation zone, is either near or larger than the Roche-lobe radius, $R_d/R_L \geq 1$.

The wind acceleration zone is defined as

$$R_d = \frac{1}{2} R_* \left(\frac{T_{eff}}{T_{cond}} \right)^{2.5} \quad (2.2)$$

where R_d is the wind acceleration radius, R_* is the primary star radius, T_{eff} is the effective temperature of the primary star, and T_{cond} is the condensation temperature of the dust. The condensation temperature is related to the chemical composition of the dust. The approximate condensation temperature of the dust grains is $\approx 1000 - 1500$ K and it is associated with the distance of the star's center.

If the dust compound is carbon-rich dust ($C/O > 1$) the condensation temperature is $T = 1500$ K, if the dust is oxygen-rich dust ($C/O < 1$) the condensation temperature is $T = 1000$ K.

Figure 2.4 illustrates the wind acceleration zone, i.e. dust formation area, of the primary star, Roche equipotential surfaces of the binary system, and the L1 point in the system's orbit.

Wind Roche Lobe overflow

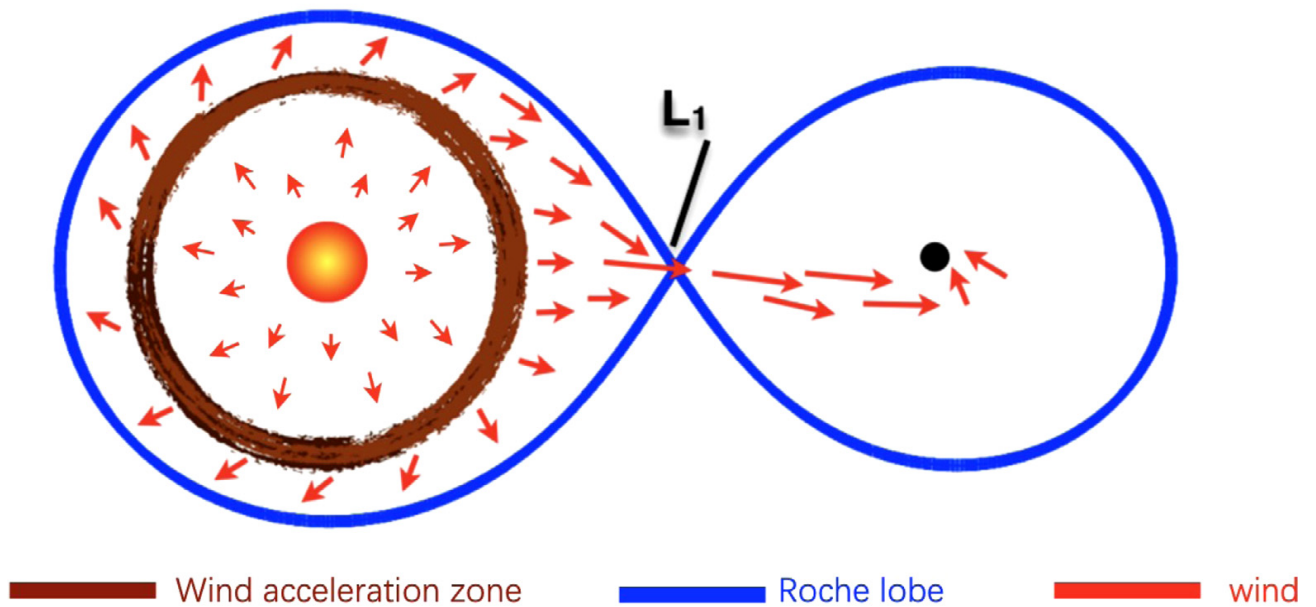


Figure 2.3: Schematic view of WRLOF in binary systems, wind acceleration zone, and formation of an accretion disk around the WD adopted from Figure 3.8 of X. Chen et al. (2023)

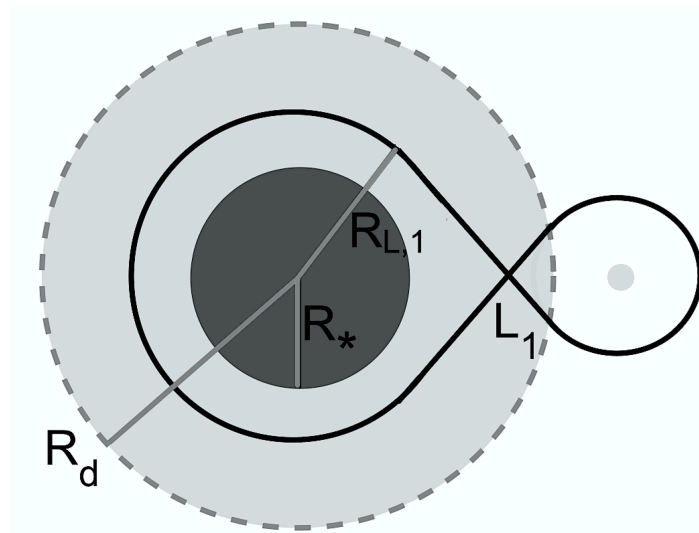


Figure 2.4: Schematic view of L1 point and the wind acceleration zone of the orbit in binary systems adopted from Figure 1. of C. Abate et al. (2013). R_d represent the wind acceleration radius, $R_{L,1}$ represent the Roche-lobe radius of the giant, R_* represent the radius of the primary star, and L_1 is the Lagrange1 point of the orbit. The radii are not to scale.

2.3. OUTBURSTS IN SYMBIOTIC SYSTEMS

The light curves of symbiotic systems are crucial for understanding the radiation that comes from each component and the surrounding nebula of the system. Their light curves show two distinct features. They are called active and quiescent phases. In a quiescent system, the ionization of wind particles and the accretion rate remain constant. The light curve shows wave-like orbital-related profile caused by rotating binary with extended and partially thick nebula in quiescent phase. The giant's mass loss can be up to about $10^{-7} M_{\odot} \text{ yr}^{-1}$ in quiescent phase. In the active phase, accretion and mass loss are not in equilibrium, leading to an increase in the accretion rate and mass outflow from the system. The system's light curve can show eclipses during this phase.

The differences in the light curves are the result of outbursts that detected in systems with a time interval of years, decades, or much more time. These two distinct phases of the light curve are further divided into accreting-only and H-burning symbiotic systems. If the transferred matter becomes degenerate on the surface of the WD, it can lead to thermonuclear explosions, resulting in a burning symbiotic system. On the other hand, if the accretion is slow and in thermal equilibrium nuclear explosion does not occur and the system is called an accreting-only system. In the accreting-only systems' optical spectra are dominated by the red giant whereas in burning-type systems' spectra are dominated by the strong nebular continuum and rich emission lines.

Accretion processes or thermonuclear instabilities in the system can cause different types of outbursts. Three different types of outbursts are observed in SySts: classical symbiotic outbursts (Z And-type), recurrent novae, and slow 'symbiotic' novae. While recurrent novae and symbiotic novae-type outbursts are associated with the thermonuclear events triggered by accumulating matter on the surface of the white dwarf, Z And-type outbursts are initiated by an increase in the accretion rate caused by expansion of the H-burning envelope or ejection of optically thick material from the WD. Slow nova outbursts occur in systems where WD masses are low ($0.6 M_{\odot}$) and there is H-burning on the surface of the WD in thermal equilibrium. These novae have slow rises, few years, to a maximum in light curve and last decades to centuries. Recurrent novae outbursts occur in systems with WD masses near Chandrasekhar limit ($1.4 M_{\odot}$) with an thermonuclear runaway event. This type of outbursts rises rapidly in a few minutes to a maximum luminosity and lasts weeks to months. If

the accreting WD is massive and the accretion rate is high, thermonuclear outburst may be repeated. Z And-type type outbursts shows increase 1-3 mag in optical band and last weeks to years.

Recently two subclasses have been added to Z-And-type outbursts. These are 1st-type (warm-type) outbursts and 2nd-type (hot-type) outbursts. This classification is based on the orbital inclination of the system. In both types of outbursts, a strong nebular continuum is present in their optical spectra. However, in the 1st type, this is accompanied by a low-temperature ($\approx 1 - 2 \times 10^4$ K) pseudo-photosphere, whereas in the 2nd type, it is accompanied by a high-temperature (≈ 165000 K) stellar component. 1st-type outbursts are seen in systems with high orbital inclination and 2nd-type of outbursts are seen in systems with low orbital inclination.

2.4. JETS IN SYMBIOTIC SYSTEMS

Jets are highly fast plasma ejections from systems that are quite common features in astrophysical sources such as Active Galactic Nucleus (AGNs), X-ray binaries (XRBs), and Young Stellar Objects (YSO). In a binary system, the origin of the jets is usually related to an accretion disk.

While jet-like structures have been observed in white dwarf systems with accretion discs, they are not a common feature of symbiotic stars, and there are only a few examples in CV systems. Only 10% of the known symbiotic stars have bipolar jet ejections.

In 2004, M. Livio found that the ratio of the observed jet velocities to the escape velocities of the central stars is nearly one for various types of systems, including symbiotic systems, YSOs, GRBs, XRBs, and AGNs. This finding supports the view that these jets originate from the accretion disk. The accretion rate is the another key point to jet ejections. In 2004, N. Soker & J. P. Lasota calculated the minimum accretion rate for jet production to investigate the reason for the absence of jets on CVs. They found that to produce the jet, the critical mass accretion rate was to be $\approx 10^{-6} M_{\odot} \text{ yr}^{-1}$ for white dwarfs. If the rate is below this value, the jet will not be produced.

The jet formation mechanism in symbiotic stars is thought to be similar to other systems that exhibit jets. In 1982, R. D. Blanford & D. G. Payne introduced the mechanism of collimated jet formation from an accretion disk through a magnetic field by solving the magnetohydrodynamic equations for cold magnetospheric flow from a Keplerian disc. According to this model, if the magnetic field's poloidal component forms a specific angle ($< 60^\circ$) with the disk, the gas flowing through the accretion disk is driven by centrifugal force and ejects. The toroidal component of the magnetic field becomes crucial, collimating the outflow into anti-parallel jets perpendicular to the disk. Close to disk, gas pressure in a hot magnetically dominated corona likely drives the flow. This model has been further developed by many other studies.

In 2003, N. Soker & O. Roger suggested a new jet ejection mechanism, for YSOs, that accelerate the flowing gas through the disk and collimate it for only small magnetic fields. Before delving into this mechanism, it is essential to define the boundary layer. Systems with a low magnetic field and a high accretion rate, the accretion disk can be extended to the surface of the accretor. The boundary layer is the zone from inner part of the accretion disk to the surface of the accretor. In this zone, with the extreme conditions, dissipation of accretion flow, and rapid variations is occur. The angular velocity of the flow (Keplerian velocity) drops to the slow angular spin rate of the star. Since the flow velocity is highest in this region, it is likely to cause shocks and instability. This mechanism suggests that thermal pressure in Spatio-temporal Localized Accretion Shocks (SPLASHs) which occurs during a brief dissipation event, a small quantity of accreted material undergoes shock, in the boundary layer (BL). The support provided by rotation against gravity is substituted by thermal pressure. Around half of the potential energy gained is emitted within boundary layer, while the remaining half has already been dissipated within the accretion disk.

Jet velocities in symbiotic systems range from 200 km s^{-1} to 2000 km s^{-1} . Although jet structures are rare in symbiotic stars, they have been observed in several types of symbiotic stars, i.e. S, D, D' -types. R Aqr and CH Cyg are the first symbiotic stars in which jet features were observed. R Aqr is a D-type system, and CH Cyg is an S-type system. Z And is known as the prototype symbiotic star with the highest magnetic field. The magnetic field plays a crucial role in the formation of the jet. The dissimilarity between them requires a more detailed study of symbiotic jets.

2.5. SHOCKS IN SYMBIOTIC SYSTEMS

Rapid changes in the thermodynamic behaviour of a plasma can give rise to shocks. These occur as a transition layer when the velocity of the plasma exceeds the speed of sound.

As the WD burns the captured hydrogen on its surface, periodic hydrogen flashes occur on the WD. This eruption cause increase in flux and radiation pressure thus WD intend to eject its hydrogen atmosphere as a form of stellar wind. This wind has high velocity with $1000 - 3000 \text{ km s}^{-1}$. As already mentioned before the primary of the system experience low velocity, $10 - 30 \text{ km s}^{-1}$, wind outflows. The interactions and collision between the high velocity WD winds and low velocity giant winds cause the shocks. The winds interact on a boundary and form an “initially” spherical nebular shell around the WD. Over time the nebular shell deformed such as shown in Figure 2.5 as the slow wind of the primary does not allow the shell to expand in the direction of the primary. The shell gather material from both winds and flow outward to the nebula. The winds of WD and giant are supersonic thus this will form shocks at both sides of the interaction region. The material moves away with supersonic velocity from the system its create an interaction region with wedge shaped. The collision of winds result in soft X-ray emission. Cwb in Figure 2.5 represents the direct interaction of the winds of the hot and cool components, and Cwc represents the low velocity wind of the primary being overtaken from the inside by the higher velocity wind of the secondary.

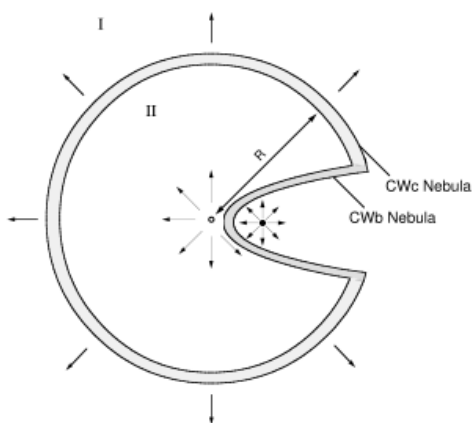


Figure 2.5: Schematic representation of symbiotic colliding winds. The open and filled circles indicate the WD and giant components of the system, respectively. The surrounding medium (I) is constituted by mass lost by the cool component before the initiation of the hot component wind (II). Cwb represent the binary colliding winds and Cwc is concentric colliding winds. Figure is adopted from Figure 1. of Kenny et. al. 2005.

The other process that create shocks in symbiotic system occur on the surface of the matter accreting star. As matter flow in the accretion disk from primary to the WD, the accreted gas when near surface of WD, has supersonic velocities which is close to free-fall velocity but its velocity makes a transition to subsonic velocities on the stellar surface to accrete material to the WD. This transition in velocity creates discontinuity in the fluid and resulting a shock. The hard X-ray emission from symbiotic stars are generally coming from inner accretion disk.

Shocks can be considered the plane parallel transition layer in a plasma. This transition layer is between the pre-shock region and the post-shock region. In these regions Rankine-Hugoniot jump conditions are described by the conservation laws. The conditions contain conservation of momentum, mass and energy. The conditions provide the post-shock conditions according to pre-shock conditions. The equilibrium between post- and pre-shock parameters can be defined in three equations.

$$\rho_1 v_1 = \rho_2 v_2 \quad (2.3)$$

$$P_1 + \rho_1 v_1^2 = P_2 + \rho_2 v_2^2 \quad (2.4)$$

$$\frac{1}{2} v_1^2 + \frac{5 P_1}{2 \rho_1} = \frac{1}{2} v_2^2 + \frac{5 P_2}{2 \rho_2} \quad (2.5)$$

where ρ is density, v is velocity and, P is pressure. The following equations can be derived from the condition equations;

$$\frac{v_2}{v_1} = \frac{1}{4} \quad (2.6)$$

$$\frac{\rho_2}{\rho_1} = 4 \quad (2.7)$$

$$P_2 = \frac{3}{4} \rho_1 v_1^2 \quad (2.8)$$

Using the equation 2.8, the equation of the shock temperature can derive with ideal gas law which is $P = \frac{\rho k T}{\mu m_H}$.

$$T_2 = \frac{P_2 \mu m_H}{k} \quad (2.9)$$

Subsequently, if the P_2 value is expressed in accordance with the notation of 2.8, the post-shock temperature can be determine as

$$T_2 = \frac{3}{16} \frac{\mu m_H}{k} v^2 \quad (2.10)$$

where μ is the mean molecular weight, m_H is the mass of the hydrogen atom, and k is the Boltzmann constant. The mean mass of a particle for a gas is given by μ , where μ is expressed in units of m_H . For neutral hydrogen, $\mu = 1$, while for a fully ionised hydrogen, $\mu = \frac{1}{2}$. The value of μ depends on the ionisation state of the gas, with different cosmic abundances resulting in values between 1 and $\frac{1}{2}$. This equation (2.10) enables the velocity of a shock wave to be calculated from the temperature of the post-shock region or visa versa.

2.6. SYMBIOTIC STARS IN X-RAYS

Since in this thesis we are studying the variation of R Aquarii in X-rays, it is useful to look at the behaviour of symbiotic stars in the X-rays.

The diversity of symbiotic systems have also been revealed in X-rays. In 1997, Murset analysed the ROSAT data of symbiotic systems and classified them into three groups based on their X-ray characteristic. The three types, α , β , and γ , represent systems with different energy distributions with increasing energies, respectively. α systems have super-soft distributions with energies below 0.4 keV. β systems have a peak at 0.8 keV with more harder radiation than α type distributions. γ systems represent systems with the highest

energies.

As the study was based on ROSAT data with an X-ray energy range of 0.2 - 2.5 keV, it was unable to consider white dwarf (WD) symbiotic systems that display very hard, heavily absorbed X-ray spectra, as well as systems that exhibit both soft and hard X-ray spectral components. Therefore, in 2013, G. J. M. Luna et al. revised this classification by adding two new types. The classification at present is as follows:

α -type: Extremely soft X-ray sources that have energies below 1 keV, with most having energies below 0.4 keV.

β -type: Soft X-ray emitting sources, usually with energies below ~ 2.0 keV.

γ -type: Symbiotic X-ray binaries with an X-ray spectra mostly above 1 keV, typically $E_x \geq 1$ keV.

δ -type: Highly absorbed hard X-ray sources emitting thermal radiation above 2.4 keV.

β/δ -type: WD symbiotics exhibiting two distinct X-ray thermal components containing both β and δ types.

Currently, approximately 20% of known symbiotic systems exhibit X-ray emission. In α -type systems, the X-ray emissions are thought to originate from quasi-steady H-burning on the WD surface. In β -type systems, the origin of the X-ray emissions are thought to be from colliding winds or jets. The plasma is optically thin and has temperatures of approximately $\sim 10^6$ K.

The X-ray emission is believed to originate from optically thick Comptonized plasma associated with SyXBs in the γ -type. In the δ -type, the X-ray emission most likely originates from an optically thin boundary layer (BL) between the accretion disk and the WD. In the β/δ -types, where WD symbiotics belong to, the soft X-ray component is thought to originate from colliding winds, while the hard X-ray component is thought to originate from the BL.

The toroidal-like density structure around the symbiotic system, the accretion disk and the jet features designating the X-ray emission types for different viewing angles are shown in Figure 2.6.

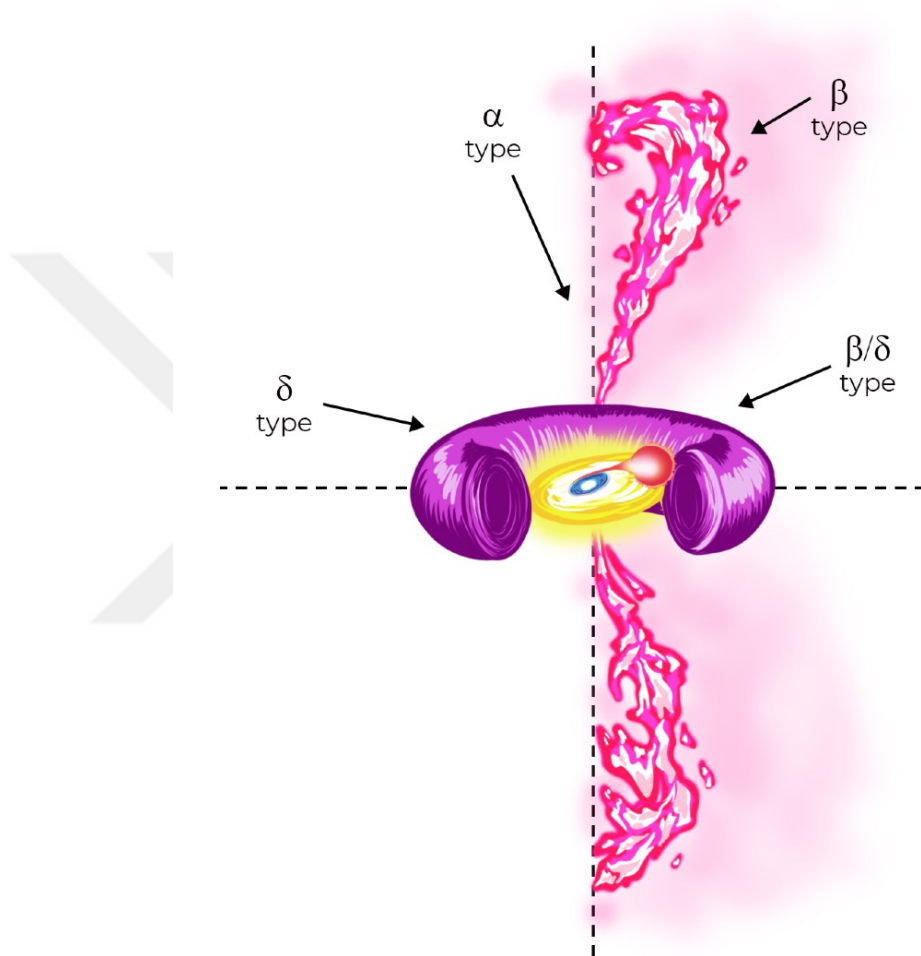


Figure 2.6: A schematic view of the structure around a symbiotic system, with the binary and accretion disk at the center adopted from Figure 7. of J. Toala (2024). The system without extended emission is on the left side of the vertical dashed line, while the system displaying bipolar ejections or jets is on the right side. Line of sights are indicated by the black arrows and labels (α - β - δ - β/δ). Sketch is not to scale.

2.7. A LOOK INTO A GLORIOUS SYSTEM: R AQR

R Aqr was first identified as a variable star by Karl Ludwig Harding in 1810. However, Korean records from A.D. 1073 and A.D. 1074 mention a star, coinciding with the coordinates of R Aqr, indicating outburst activity that is now thought to have formed its current surrounding nebula. The nebula surrounding the R Aqr system is also known as Cederblad 211. It was named after S. Cederblad, who identified it in his 1946 thesis on diffuse galactic nebulae. Systematic observations of R Aqr began in the early 20th century. The system's orbital parameters have been extensively studied through multiwavelength observations. Additionally, the proximity of the system, ~ 218 pc, to the Earth has contributed for studies on the system.

R Aqr belong to D-type symbiotics. It consists of an M-type Mira variable star as its primary component, which pulsates over a long period of ~ 387 days and has a mass of $\sim 1 - 1.75 M_{\odot}$. Its companion is a white dwarf with a mass of $\sim 0.5 - 1.4 M_{\odot}$. They are surrounded by a nebula with an hourglass shape. The nebula extends to ~ 2 arcmin in E-W directions and ~ 1 arcmin in N-S directions from the central binary. The effective temperatures of the Mira and the WD are ~ 2800 K and ~ 40000 K, respectively. R Aqr has orbital period of ~ 43.6 yr with an eccentric orbit, i.e. $e = 0.25$, and the semi major axis, a , is ~ 15 AU. Binary separation of the components is ~ 9.8 AU. The radius of an accretion disk around the secondary (WD) is ~ 5 AU.

R Aqr is characterized by a complex structure involving colliding winds in the system, mass accretion onto the secondary, bipolar jet outflows, and a surrounding nebula of the system. These elements contribute to the dynamic nature of the system. Although jets are relatively uncommon in SySts, R Aqr exhibits bipolar outflows. It is believed that the jets are one-sided and alternate direction roughly every decade. The first jet structure of R Aqr was detected in the optical wavelength observations in 1977, 6" away from the binary in the NE direction. While there was no consensus on the origin of the jet outflows, it is postulated that they are linked to the periastron passage of the system. During periastron the WD accretes matter from the Mira at its maximum rate results in the ejection of collimated material from the accretion disk. At this point that should be consider if the jet is ejects nearly one in a decade the origin of the jets can not be just periastron. The jets of R Aqr have been the subject of study at many different wavelengths, as the origin and periods of jet activity provide insight

into the nature of the system.

In 1979 and 1980, X-ray observations of R Aqr was made with the EINSTEIN telescope, but no source was detected at the location of the central binary. Hence, the first official detection of R Aqr and its jets in X-ray was made in 1985 with EXOSAT. Subsequently, further X-ray observations were conducted. In 2000, R Aqr was observed with *CHANDRA* revealing the presence of two-sided jets directed towards the NE and SW from the central binary for the first time in the X-rays. It is found that the X-ray emission comes from the central region and jet structures. Fe $K\alpha$ line at 6.4 keV was found on the central region spectrum. The origin of the Fe $K\alpha$ line in the inner part of the accretion disk in the vicinity of the central compact source, supports the accretion onto a WD scenario in the system. They used non-ionization equilibrium plasma models to model both jet spectra and found the corresponding ages of the jets to ~ 10 years or less. A subsequent 2004 *Chandra* observation revealed that the NE outer jet exhibited a change in position with an apparent velocity of $580 \times (d/200) \text{ km s}^{-1} \pm 30 \times (d/200) \text{ km s}^{-1}$ over the 3.3 years. Here, d refers to the distance to the R Aqr. They also revealed that X-ray emission from SW outer lobe-jet faded by 75% overall compared to previous observations. This could be due to adiabatic expansion or cooling. In addition to these findings, we present in this thesis the analysis of the recent *Chandra* data of R Aqr covering the years 2017, 2020, 2021, and 2022. The analysis in this thesis was completed before A. Sacchi et al. 2023 which involves these data sets. However, the analysis in this thesis have a different approach.

In addition to X-ray observations, R Aqr has also been studied in radio, infrared, and optical wavelength. In 2014, R Aqr was observed with two optical telescopes: Hubble Space Telescope (HST) and the Very Large Telescope (VLT) with the SPHERE-ZIMPOL instrument. Figure 2.7 shows the HST Ha image with the size 45" x 45" exhibiting extended emission up to 20" in the NE and 30" in the SW directions. The image shows curved lobes formed by bright emission arcs. The authors pointed out that this curvature suggests that the central object is rotating counterclockwise. The central binary of R Aqr has been resolved thanks to the high resolution, $\sim 20 - 30$ mas, of the SPHERE/ZIMPOL instrument. These observations suggest that the origin of both jets are located to the east of the central binary and outflow follows a curved path in the initial sections. However, while the NE flow then forms a straight pattern, the SW flow is very distorted and follows a "zig-zag" pattern. Figure 2.8 illustrates the narrow-band H α image. The image displays the inner SW jet, the shifted

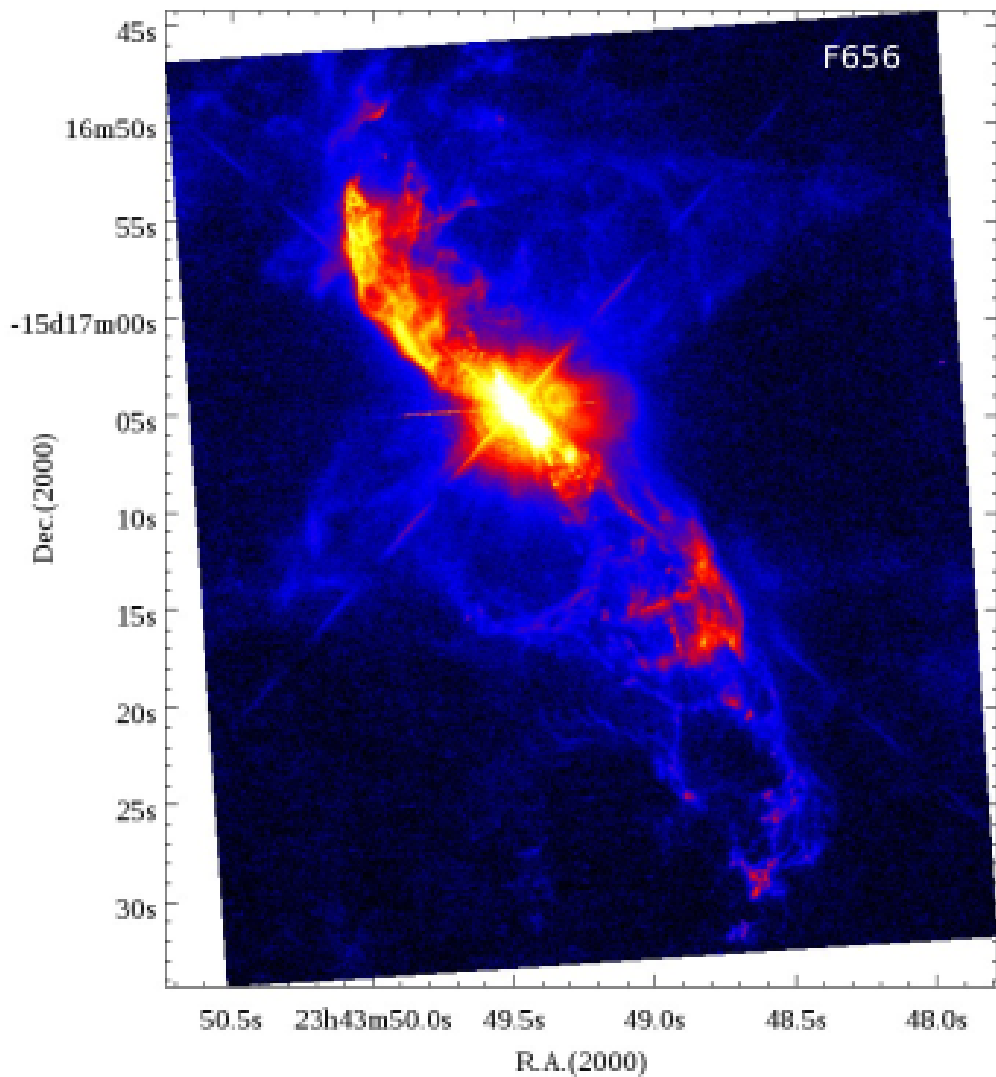


Figure 2.7: HST image of R Aqr with a scale of $\sim 45'' \times 45''$ taken with $H\alpha$ filter on October 18, 2014 adopted from Figure 1. of Melnikov et. al. 2018.

initial section of the SW jet compared to the NE jet and the curvature of the gas counter flows.

Optical observations provide insights into the complex structure of R Aqr, while the eclipses highlights dynamic changes within the system. Future observations help to understand the evolutionary processes of the R Aqr more effectively.

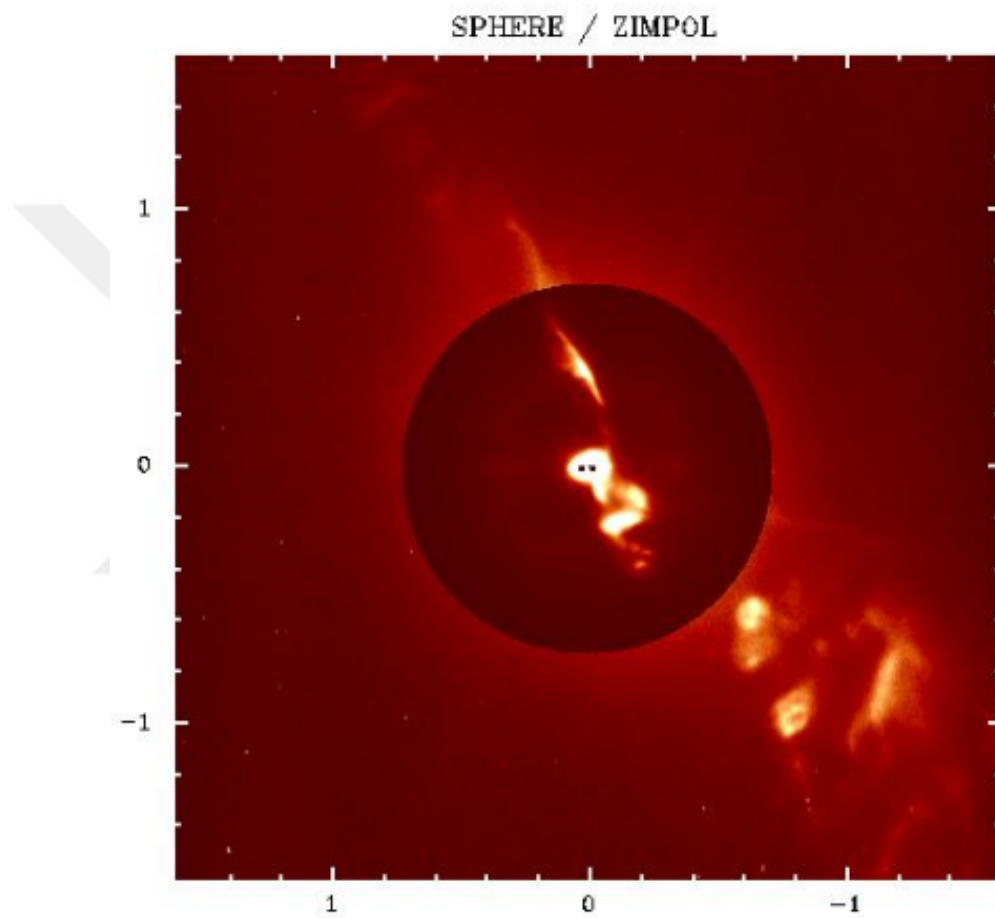


Figure 2.8: Narrow-band H α image of R Aqr from VLT/SPHERE-ZIMPOL with a scale of $70'' \times 70''$. $3''.5 \times 3''.5$ central area is indicated with the circle and the central binary is marked with two dots. Image taken on October 2014 and adopted from Figure 1. of Schmid et. al. 2017.

Analysis of the light curve of Mira-type primary has revealed that it undergoes periodic eclipses, characterized by an increase in minimum brightness and a decrease in maximum brightness. Although a decrease in its brightness was observed around 1930, on the light curve for observations between 1920 and 1934, the first recorded eclipse was in 1978. The contributions of the subsequent observations indicate that Mira-type primary is eclipsed by an opaque body or accretion disk approximately once every ~ 44 years. This is identified as a disk eclipse and reveals that primary pulsation was observable during the eclipse which points out that this is not a total eclipse. The duration of the eclipse is found to be less than 8.5 years. Although the forthcoming eclipse is expected to occur in 2022, it has been reported that it began in 2019. R Aqr was observed with SOFIA/FORCAST and found that after the outset of the eclipse a decrease in optical brightness and an increase in mid-IR flux were observed. The increase in the mid-IR flux is due to the changing distance between the WD and the Mira-type primary, which affects the dust density in the outflow. The eclipses presents an opportunity to study the accretion disk, which is occulting the Mira. Figure 2.9 showing broad and narrow band $H\alpha$ images of R Aqr taken in 2014 with VLT/SPHERE-ZIMPOL, points out the compact emission region around the WD. The broadband image (left-hand side on the figure) displays the Mira, while the narrow-band (right-hand side on the figure) image reveals an additional compact emission region around the active companion, which is thought to be the origin of jets. The narrow-band $H\alpha$ image was taken when the optical brightness of the Mira-type primary was at minimum phase.

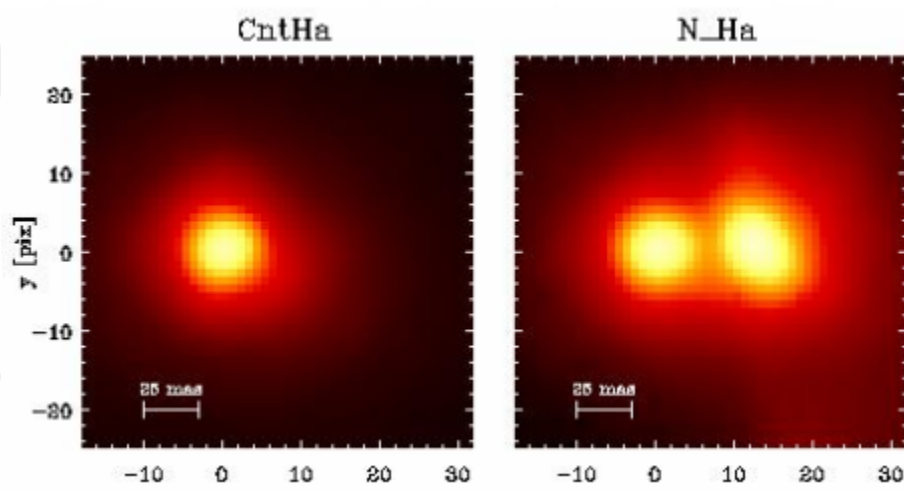


Figure 2.9: Left: Broadband $H\alpha$ image of R Aqr taken on October 11, 2014, with VLT/SPHERE-ZIMPOL telescope. Right: The first resolved image of the R Aqr was obtained when the Mira was at its minimum brightness on October 11, 2014, using the Narrow $H\alpha$ filter on the VLT/SPHERE-ZIMPOL telescope. Images adopted from Figure 4a-4b of Schmid et al. 2017.

3. MATERIAL AND METHODS

3.1. X-RAY OBSERVATIONS

3.1.1. Chandra X-Ray Observatory

The *Chandra X-ray Observatory* (CXO) was launched on July 23 1999 by NASA. It completes an elliptical orbit around the Earth in approximately 64 hours and 18 minutes. Since its launch, *Chandra* has become one of the most outstanding X-ray telescope. *Chandra* covers 0.1 - 10.0 keV energy range. The reasons for this reputation of *Chandra* can be considered as the high sensitivity and resolution of its instruments. ACIS instrument (Advance CCD Imaging Spectrometer) has two main detectors ACIS-I and ACIS-S. ACIS-I has four front-illuminated (FI) CCD chips with 16.9×16.9 array size that are used for imaging. ACIS-S has six CCD chips two of them being back-illuminated (BI) with 8.3×50.6 array size. The pixel size of the ACIS instrument is 0.492 arcseconds.

HRC (High-Resolution Camera) has two main microchannel plate (MCP) detectors HRC-I and HRC-S that are sensitive to X-ray photons. HRC-S has a 6×90 arcmin field of view, whereas HRC-I has a 30×30 arcmin field of view. The spatial resolution and energy range of HRC is ~ 0.4 arcsec and 0.08 - 10.0 keV respectively. HETG (High Energy Transmission Grating) and LETG (Low Energy Transmission Grating) are two grating spectrometers of CXO. These spectrometers provide high-resolution spectroscopy. HETG is sensitive to 0.4 - 10.0 keV energy band and LETG is sensitive to 0.07 - 2.0 keV energy band. Unlike HETG, LETG provides high-resolution spectroscopy in the soft X-ray band. A schematic view of *Chandra* and its instruments is shown in Figure 3.1.

3.1.2. Observations of R Aqr

Since it was first observed in 1922, R Aqr has been observed at various wavelengths of the electromagnetic spectrum. R Aqr has been observed by several X-ray telescopes, including ROSAT, XMM-NEWTON, and *CHANDRA*. Despite this, it is still not fully understood. In this study, our motivation is to contribute to the investigations of R Aqr in X-rays.

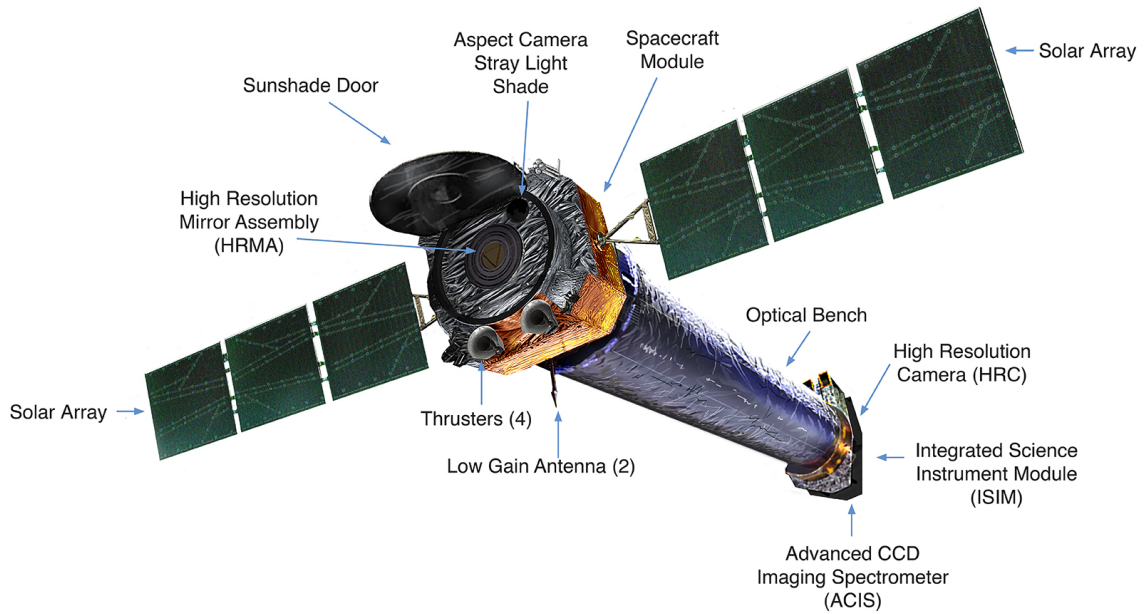


Figure 3.1: Schematic view of *Chandra* X-ray Telescope and its instruments. Image credit NASA/CXC.

The first *Chandra* observation of R Aqr was made in 2000. Other observations followed this in 2003 and 2005. These data have been studied in detail before. The most recent *Chandra* observations of R Aqr were made in 2017, 2020, 2021 and 2022. We have utilized these data sets for this thesis since the quantity and the durations would allow for a detailed study.

The data was obtained from the HEASARC database. In this thesis, *Chandra Interactive Analysis of Observations* (CIAO)¹ program was used to calibrate the *Chandra* data. The data was analyzed in two parts: morphological and spectral. To interpret the spectral and morphological variations of R Aqr accurately, we also used previous archival *Chandra* data from 2000, 2003, and 2005 (ObsID:651,4546,5438). All the data utilized in this thesis are displayed in Table 3.1.

¹ Website : <https://cxc.cfa.harvard.edu/ciao/>

Archival Chandra Data of R Aqr

Obs. ID	Start time (UTC)	Exposure (sec)	Instrument Detector	Offset (arcmin from source)
651	2000/09/10 04:58:36	24580	ACIS-S	0.003
4546	2003/12/31 15:04:37	37020	ACIS-S	0.009
5438	2005/10/09 19:08:50	70180	ACIS-S	0.034
20809	2017/10/11 08:22:21	50020	ACIS-S	0.009
19015	2017/10/13 13:48:02	76650	ACIS-S	0.009
23108	2020/01/11 23:53:56	48110	ACIS-S	0.009
23325	2021/04/29 21:38:04	32340	ACIS-S	0.001
24341	2021/04/30 18:00:36	36090	ACIS-S	0.001
27333	2022/09/26 11:53:07	27570	ACIS-S	0.001
27322	2022/10/03 18:33:27	19070	ACIS-S	0.001
27467	2022/10/04 06:14:58	20080	ACIS-S	0.001
27468	2022/10/09 17:27:37	15070	ACIS-S	0.001

Table 3.1: The data referenced in this study.

3.2. IMAGE PROCESSING

The spatial images of R Aqr were generated using the *dmcopy* task within *Chandra Interactive Analysis of Observations* (CIAO), Version 14.15.2. SAOImageDS9 (Version 8.5)² was utilized for visualization, smoothing, and other related analysis.

Since several observations were made in the same year, the observations with the longest exposure time were selected for imaging. The observation ID, of these observations are 19015 (2017), 23108 (2020), 24341 (2021), and 27333 (2022).

3.2.1. X-ray Emission Morphology

Once the data was collected, the event files were reprocessed using the *repro* task within CIAO. Then a 0.3 - 10.0 keV image was created, for each epoch, from the *event2* file using the *dmcopy option = image* tool. They were centered on R Aqr, with an extracted sub-image size of 120×120 pixels, and smoothed using a Gaussian filter of $\sigma = 2''$. The spatial resolution of the images are 0.25" and the scale parameter, which adjusts the colour distribution, was set to *sqrt* to ensure uniformity among the images presented in this thesis.

² Website : <https://sites.google.com/cfa.harvard.edu/saoimageds9>

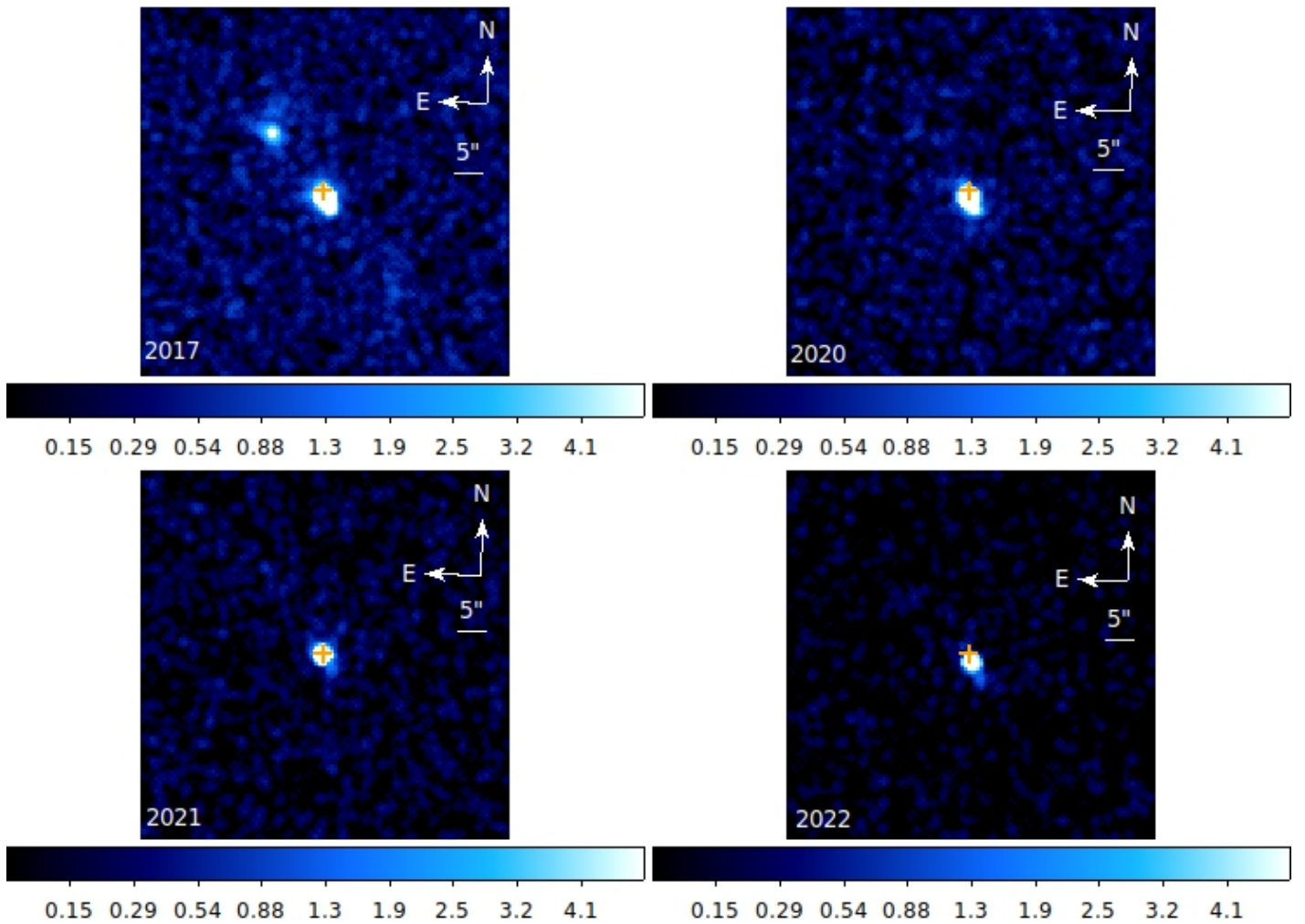


Figure 3.2: *Chandra* images of R Aqr in the 0.3 - 10.0 keV with the resolution of 0.5" pixel size. Gaussian smoothing $\sigma = 2$ pix was used for each image. The top left shows 2017 data the top right 2020 data, the bottom left 2021 data, and the bottom right 2022 data. The location of the central source is indicated by the orange cross for each image.

Images of R Aqr in the 0.3-10.0 keV are shown in Figure 3.2. The bulk of the X-ray emissions in these images are centered around the binary system and exhibit a diffuse structure. 2017 data indicated a remnant of an old jet in the NE direction and a diffuse central structure extending up to a radius $\sim 6''$ in the SW direction. This ancient jet remnant was not detecting in 2020 observation, ≈ 2 years later, and subsequent observations. The diffuse structure is still present in 2020 but much dimmer than in 2017. In 2021 X-ray emission is concentrated in the central region and is more point-like than diffuse. In 2022 the diffuse structure reappeared and the X-ray emission did not seem to be centered on the source coordinates of R Aqr.

The morphology of R Aqr was analyzed in three different energy ranges: 0.3 - 1.5 keV, 2.0 - 5.0 keV, and 5.0 - 8.0 keV. The different energy band images were calculated from the *event2* files with the *dmscopy* tool in CIAO. The same procedures applied to the broadband images were performed on these images. Figure 3.3 shows 0.3- 1.5 keV images of R Aqr revealing distinctive features in the soft X-ray emission across different epochs. The NE old jet remnant and diffuse structure were notably prominent in the broad-band image in 2017. It can be said that the soft X-ray emission in the 2017 data is similar to that observed in 2005. In the soft band image of 2020 data, the diffuse structure that oriented towards the SW direction became clearer compared with the broad-band image. A notable decrease in soft X-ray emission was observed approximately one year later in 2021. In 2022 bulk of the soft X-ray emission was concentrated in the SW direction. Consequently, the soft X-ray emission exhibited a diffuse structure extending from the central region to the SW direction $\sim 2''$ consistently across all epochs.

2.0 - 5.0 keV images of R Aqr are shown in Figure 3.4. In the three epochs, the mid-band images consistently showed a concentration of X-ray emission around the central region with a point-like shape, indicating the dominant emission source within the system. However, in the 2022 data, a deviation from this pattern is observed, with the X-ray emission being distinctly centered in the SW direction, but a point-like structure is observed in this one, as well.

The images of R Aqr in the hard X-rays between 5.0-8.0 keV is shown in Figure 3.5. Compared to other years, the 2017 data indicate a more diffuse structure around the central region. We caution that 2017 data has the longest exposure and the most number of photons. This situation marks a change in the system. As in the mid-band X-ray images, the high-band X-ray images also show that the emission in the 2022 data is not centered close to the position of the binary system, but is centered in the SW direction. As in 2022 in 2017 and 2020 bulk of the emission is not centered on the position of the binary.

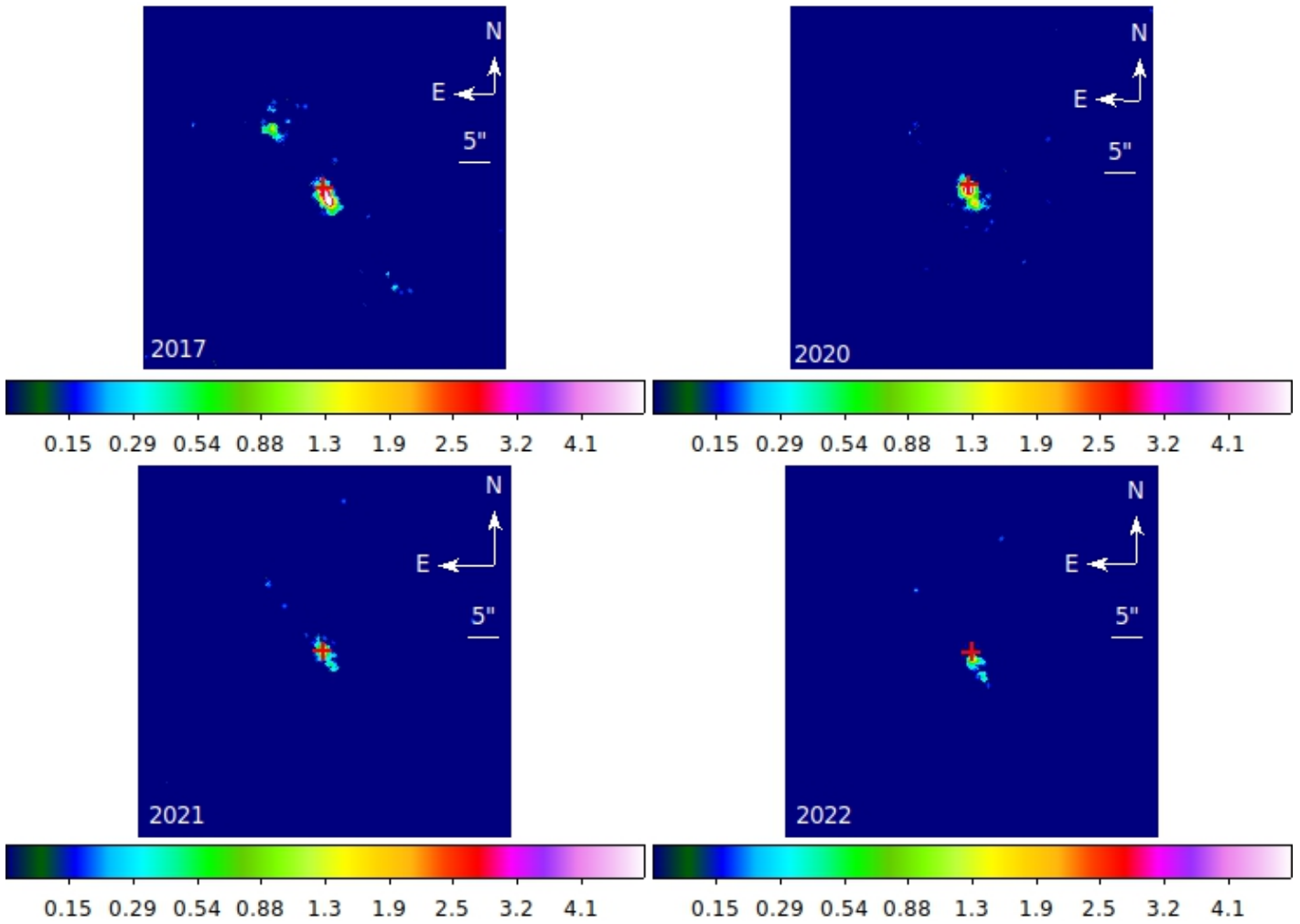


Figure 3.3: Images of R Aqr in the 0.3-1.5 keV range with $0''.25$ pixel size. Colormap and scale parameters are identical in all the images. Gaussian smoothing $\sigma = 2$ pix was used for each image. The corresponding year is indicated at the top left of each image. The red cross sign indicates the location of the central binary system.

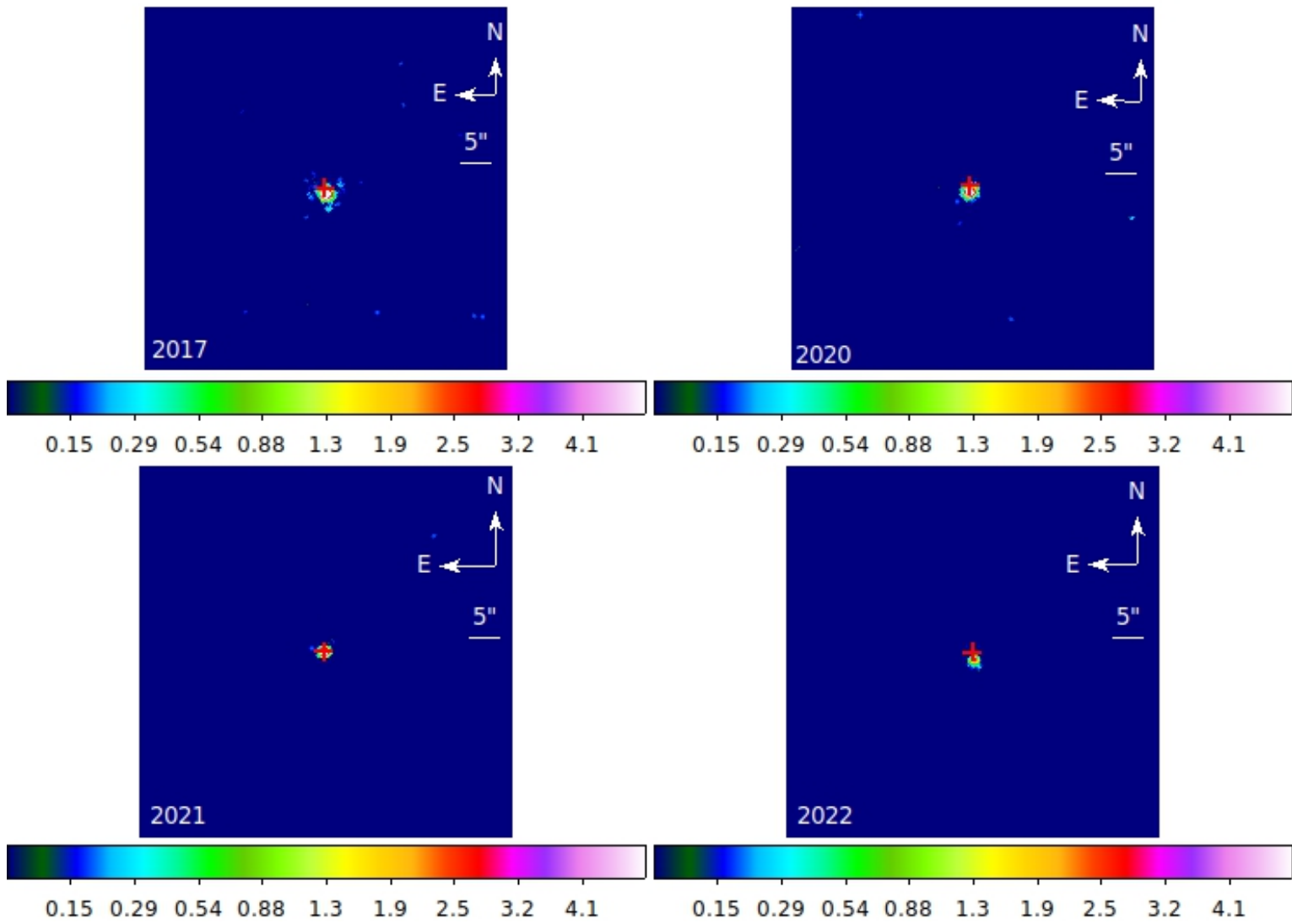


Figure 3.4: Images of R Aqr in the 2.0-5.0 keV range with $0''.25$ pixel size for each year. Gaussian smoothing $\sigma = 2$ pix was used for each image. The corresponding year is indicated at the top left hand side of each image. The location of the central source is indicated by a red cross sign.

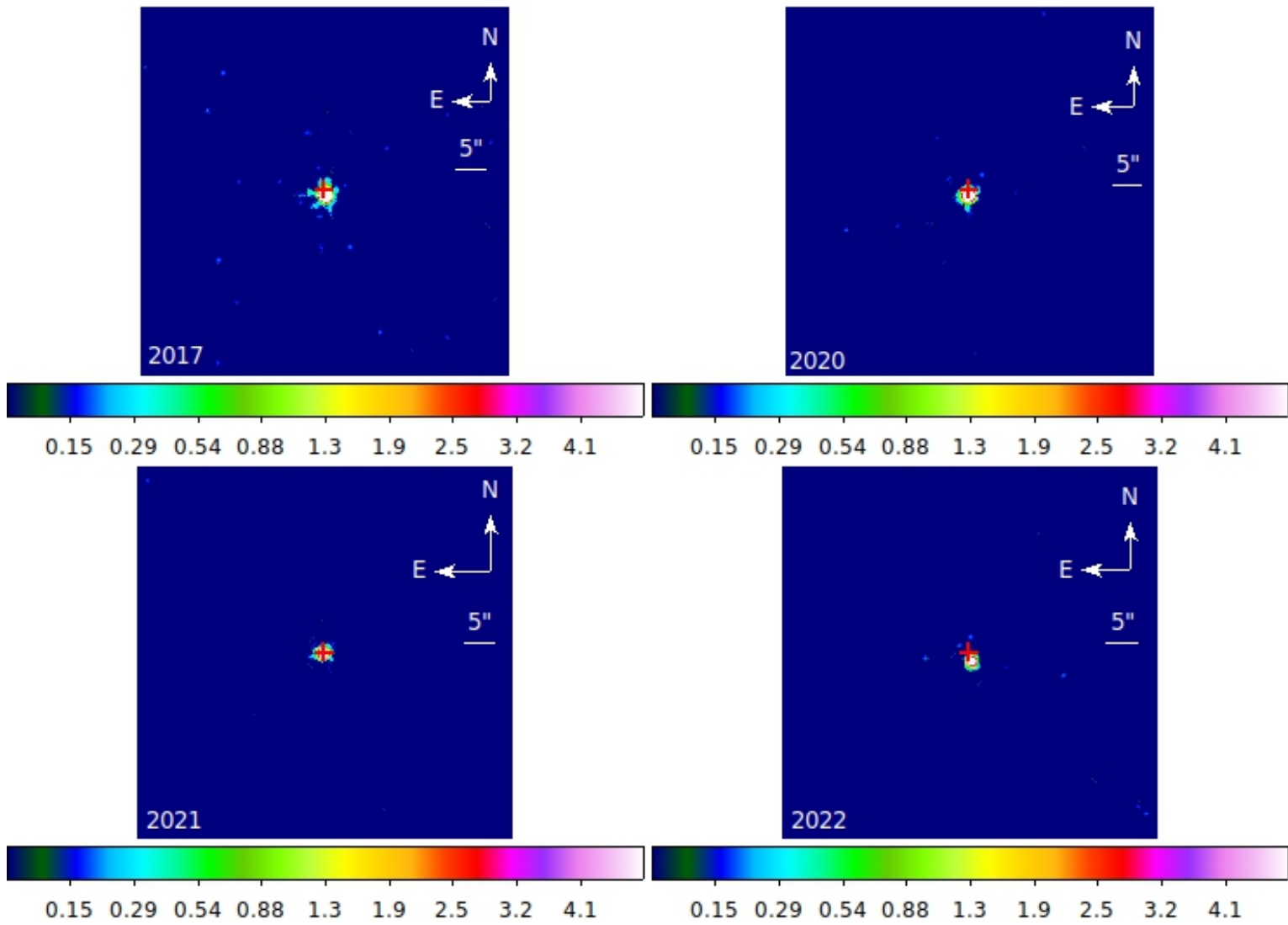


Figure 3.5: Images of R Aqr in the 5.0 - 8.0 keV range with a resolution of 0.25'' for each year. Gaussian smoothing $\sigma = 2$ pix was used for each image. The corresponding year is indicated at the top left hand side of each image. The location of the central source is indicated by a red cross sign.

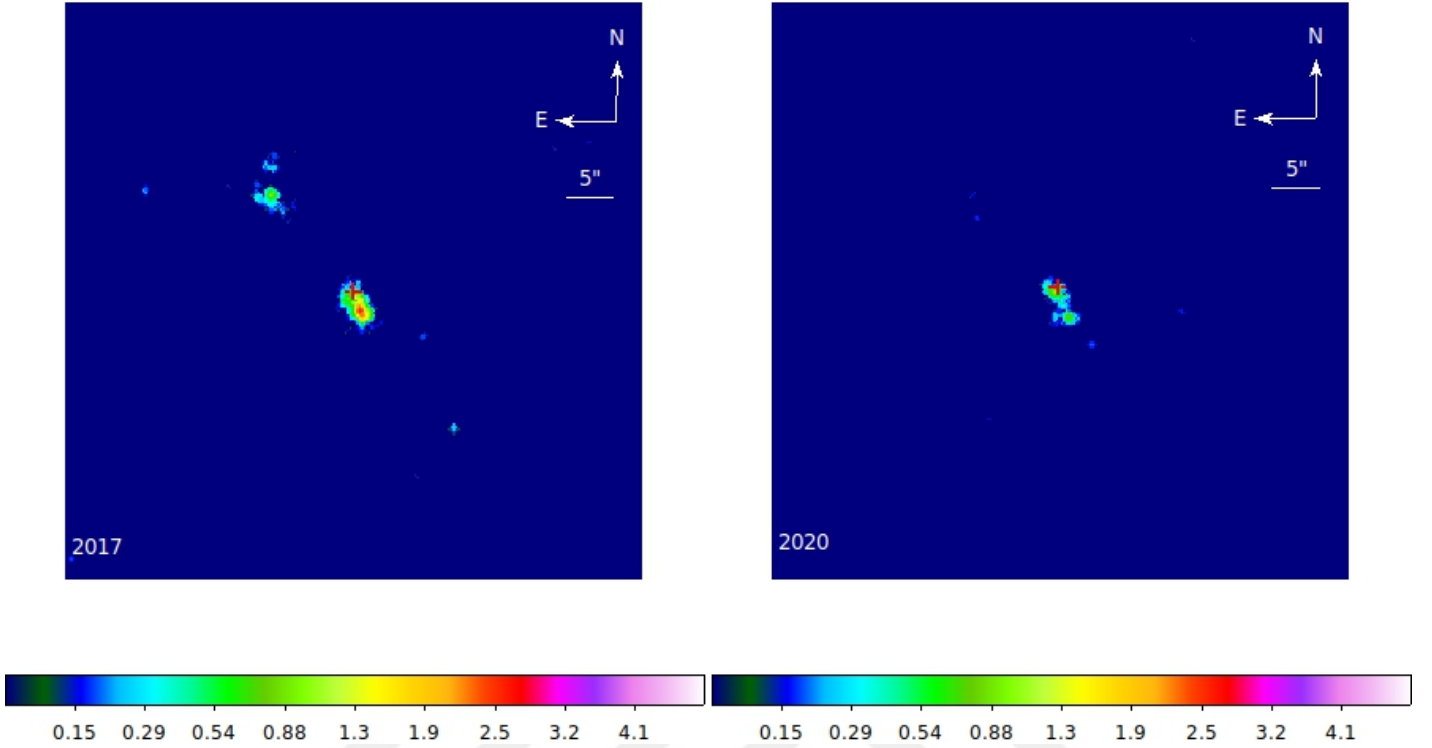


Figure 3.6: Narrow-band images of R Aqr in the 0.3-0.7 keV range for 2017 and 2020 data, respectively. Gaussian smoothing $\sigma = 2$ pix was used for both images. The location of the central source is indicated by a red cross sign.

3.2.2. Line Energy Images

0.3 - 0.7 keV narrow-band images are shown in Figure 3.6. This range covers the N VI line at 0.43 keV, the N VII line at 0.50 keV, the O VII line at 0.52 keV, and the O VIII line at 0.56 keV. In these images, we observe morphological changes from year 2017 to 2020. In 2017, the X-ray emission extended $\sim 5''$ in the SW direction from the central source and was detected $\sim 8''$ away in the NE direction, while in 2020, it extended $\sim 2''$ SW direction from the central source. In 2017, the emissions from the SW region appeared as a separate blob-like structure, similar to the soft band images of the central source region. This structure can be seen in 2020 but its shape distorted and faded compared to 2017. The NE jet remnant structure was visible in 2017, but in 2020 this structure was not observed even in the softest energy range. Therefore it has cooled off. No features were detected in this range, (0.3 - 0.7 keV), in the 2021 and 2022 data so they were not added.

3.3. SPECTRAL ANALYSIS

In order to perform spectral analysis of R Aqr, two different regions were selected for each observation to distinguish between the central region and the diffuse region in the SW direction. The initial region is a 1".5 radius circle, centered on the coordinates of the central source. The extended region is also a 1".5 radius circle and was derived in the SW direction excluding the central region (hereafter referred to as off-center). While the off-center regions exhibit minimal differences, it should be noted that they were not selected from identical locations for each observation. The center was determined based on where most of the emission comes in SW region. The exact location of central and off-center regions were shown in this thesis following parts. In addition to these two regions, a region of an 8" radius circle was selected in the 2017 data, which includes an ancient jet remnant in the vicinity of the NE direction. This structure was not analyzed in the other observations as it is non-detectable in subsequent observations. The background regions were chosen to be the same size as the source regions. The spectra of these regions were extracted using Chandra Interactive Analysis of Observations (CIAO, Version 4.11.2) with *specextract* task.

The X-ray Spectral Fitting Package (XSPEC) is a program that allows for spectral fitting that is independent of the detector. The first version of XSPEC was written by Rick Shafer at the Institute of Astronomy, Cambridge in 1983. In this thesis, the latest version of the X-ray Spectral Fitting Package (XSPEC, Version 12.13.1) was used for spectral analysis. There are three kinds of models within XSPEC. The two main models are additive and multiplicative. The last model can be described as convolution, pile-up, and mixing models. These models characterize the physical processes that produce X-ray emission from astrophysical objects. Additive components represent emission mechanisms such as power-law emission, thermal models, or emission lines. Multiplicative models are used to address additional factors that affect the observed emission, such as interstellar absorption, instrumental response functions, and background contamination. In spectral analysis, we used a composite model including additive and multiplicative model components.

The χ^2 test is the default test statistic used to calculate the goodness of fit in XSPEC. And the χ^2 can be defined as

$$\chi^2 = \sum_{i=1}^n \frac{(N_i - s_i)^2}{\sigma_i^2} \quad (3.1)$$

where n is bins of the spectrum, N is observed data, s is the expected data for the tested model, and σ is the statistical error on the measured values. Reduced chi-squared, χ_v^2 , can be defined as a measure of the goodness of fit. It described as

$$\chi_v^2 = \frac{\chi^2}{n - p} \quad (3.2)$$

where p is the number of free parameters and generally $n - p$ is called the degree of freedom (dof). The goodness of fit can be checked according to the values of χ_v^2 and the value should be approximately 1 to be considered a good fit. In other words, χ^2 must be almost equal to dof.

Cstat, known as the Cash statistic (Cash, 1979), is another statistical model used in XSPEC when the data has a low count/bin. It is defined as

$$C = 2 \sum_{i=1}^n s_i - N_i + N_i \ln(N_i/s_i) \quad (3.3)$$

For the spectral analyses in this thesis, *cstat* was used to perform the statistical test.

3.3.1. Spectra of 1".5 Region Around the Central Source

The regions shown in Figure 3.7 were selected by loading the processed fits files into SAOImageDS9. The region files with *.reg* extension were created to perform spectral extraction. Then the spectra of the central region were extracted for all the observations using the *specextract* tool. When spectra for all years have been created, they are combined according to the year with the *combine_spectra* tool. Consequently, we had four datasets for the central region. Covering years 2017, 2020, 2021, and 2022.

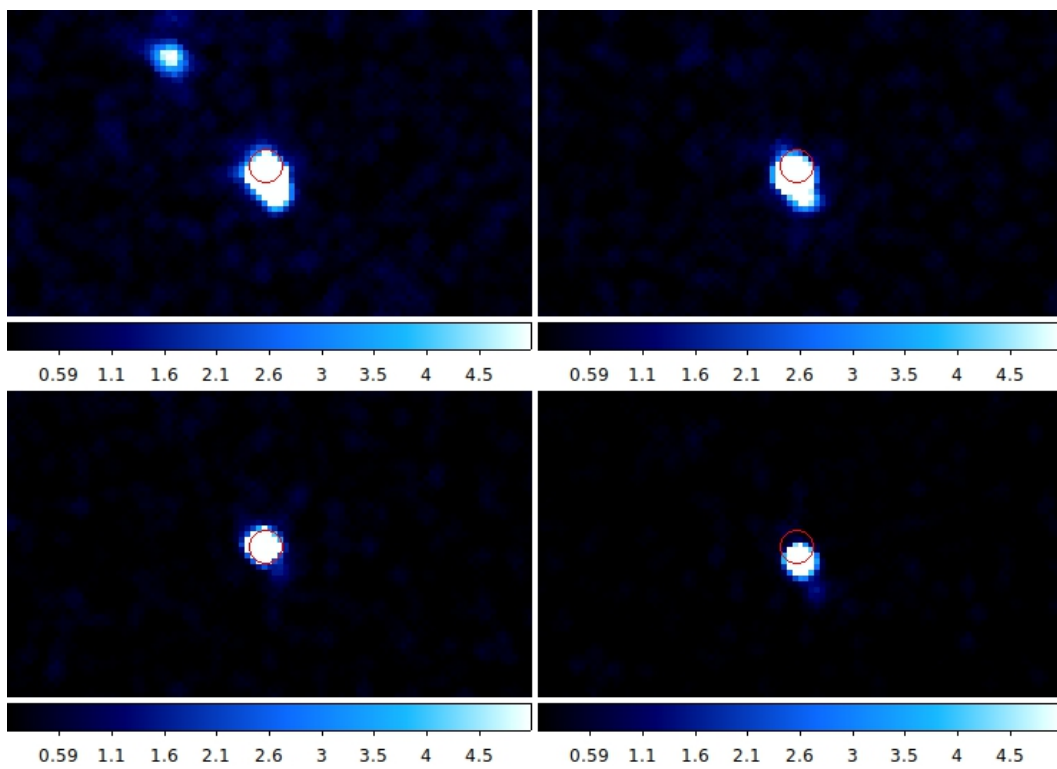


Figure 3.7: The circular regions with a radius of $1''.5$ from which the central source region spectra were taken are indicated by the red circles. The top left shows 2017 data the top right 2020 data, the bottom left 2021 data, and the bottom right is the 2022 data.

The combined spectra of the central region were binned using the *dmgroup* task with the *groupype=NUM_CTS* option in CIAO with 20 counts/bin. The central region spectrum was analyzed in the 0.3 - 8.0 keV range.

R Aqr represents an example of a β/δ type symbiotic system, characterized by an X-ray spectrum that consists of two different components, soft and hard. The hybrid nature of the spectrum in the R Aqr system is because the emitted radiation comes from different parts of the system. At least two different temperatures are required to accurately characterize the system spectrum.

For the central source spectrum fit we used two different composite models (hereafter referred to as Model1 and Model2) using the NEI (non-equilibrium ionization) plasma model in XSPEC along with different absorption models; *pcfabs* (partial covering absorber model), *tbabs* (Tuebingen-Boulder interstellar absorption), and *zxicpf* (partially ionized absorber model). In addition to these, thermal Bremsstrahlung emission model was added in the second model. Thus, Model1 is describe this formula " $tbabs \times (pcfabs \times nei + (zxicpf \times (nei + gauss)))$ " while Model2 is denoted as " $tbabs \times (pcfabs \times nei + zxicpf \times (bremss + nei + gauss))$ ".

In these two composite models, the *tbabs* model was employed for the interstellar column density, and fixed to $0.02 \times 10^{22} \text{ cm}^{-2}$ which is the value taken from N_H column density tool³ on the HEASARC website. To effectively model the central source, we initially utilized two different temperature parameters with a non-equilibrium plasma model (NEI) for both of the soft and hard components. The absorption parameter for the soft part was characterized using the partially covering cold absorber neutral material, i.e. the *pcfabs* model. For the hard X-ray part, an ionized partially covering material, i.e. the *zxicpf* model, was selected. The X-ray spectrum of R Aqr shows fluorescent Fe $K\alpha$ emission at 6.4 keV (Mushotzky et al., 1978), which is thought to originate from the boundary layer of the accretion disk. So a Gaussian model was included in the composite model for the 6.4 keV line emission. The description of the composite models are indicated in the Table 3.2 and Table 3.3.

The fitted X-ray spectra using Model1 are shown in Figure 3.8. The best-fit spectral parameters with Model1 and their errors are displayed in Table 3.2

³ Website: <https://heasarc.gsfc.nasa.gov/cgi-bin/Tools/w3nh/w3nh.pl>

In the hard part, the temperature parameter in Model1 did not deviate from the old Chandra data but was observed to be slightly higher than these values. Therefore, Model2 was derived, adding a thermal Bremsstrahlung emission component in the hard part of Model1.

The fitted X-ray spectra using Model2 are shown in Figure 3.9. The fitted spectral parameters with this model and the errors are displayed in Table 3.2.

3.3.2. Spectra of 1".5 Region Around the Off-center

To extract the off-center spectra, we selected the regions from all epochs shown in Figure 3.10. Then, we merged the spectra using the *combine_spectra* tool for the data taken in the same year. Using a similar method of analysis to the central source region, we obtained four data sets for the off-center region.

The off-center spectra were binned with 5 counts/bin using the *dmgroup* task with the *groupype=NUM_CTS* option. Due to the low count statistics, the spectra were analyzed in the range of 0.3 - 5.0 keV.

To fit the spectrum, the hard, X-ray data and part of Model1 were excluded and only the soft X-ray part was considered. The fitted X-ray spectra, the best fits parameters and their errors for the off-center region are shown in Figure 3.11. The spectral parameters are given in the Table 3.4.

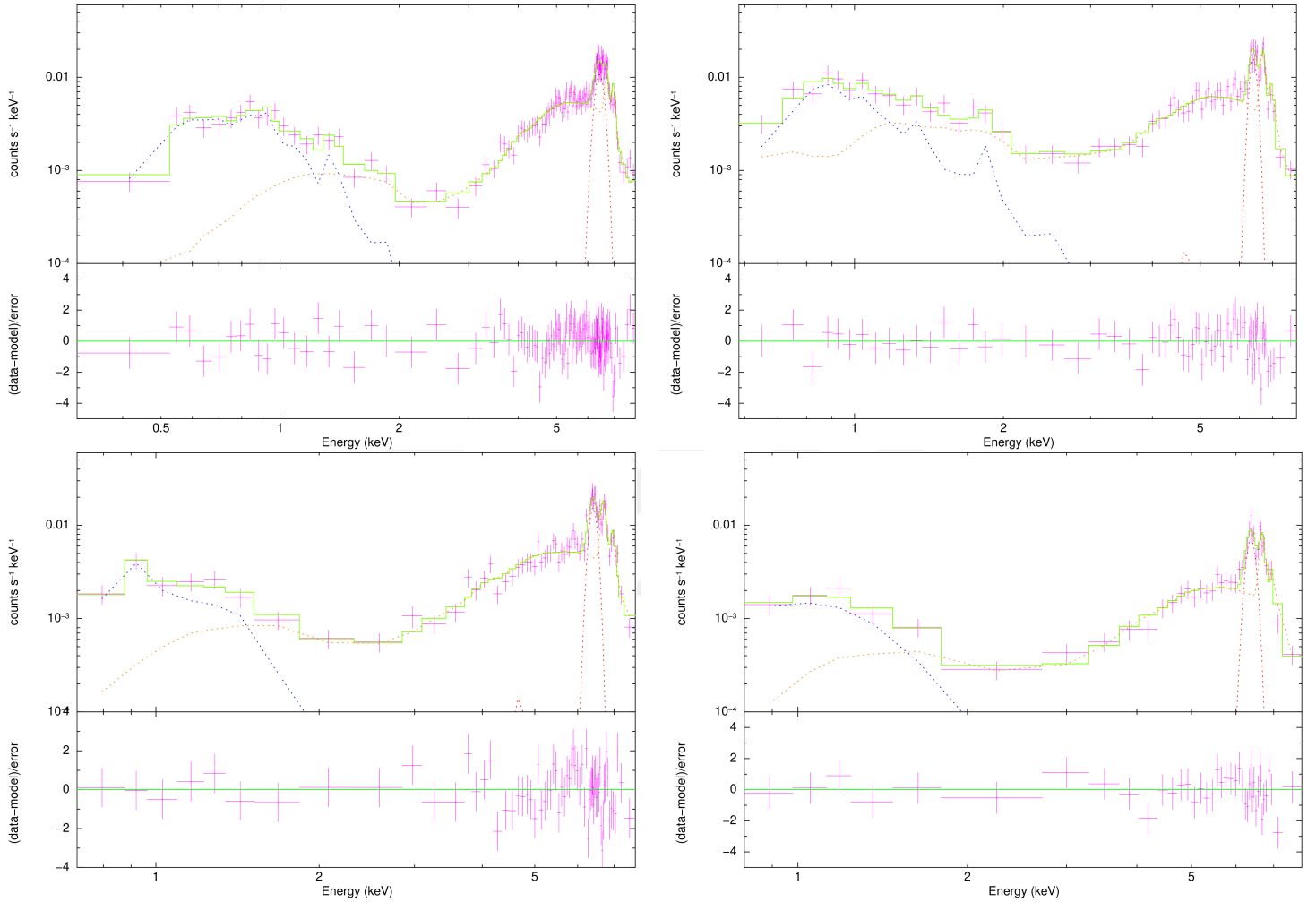


Figure 3.8: X-ray spectra and best-fit models of the $1''.5$ region around R Aqr using the Model1 in 2017, 2020 (top panel, left to right), 2021, 2022 (bottom panel, left to right). Data are shown in pink and fits are shown in green. The blue dotted lines show, the soft component and the orange dotted lines show the hard component. The Gauss line is shown in red dashed lines. The second panel of each spectrum shows the residuals of the fits in standard deviations.

Table 3.2: Spectral Fit Parameters in the 1".5 central source region.
 Model1 is used: $t\text{babs} \times (\text{pcfabs} \times \text{nei} + (\text{zxipcf} \times (\text{nei} + \text{gauss})))$

Quantity	Unit	2017	2020	2021	2022
Interstellar Absorption (N_H)	10^{22} cm^{-2} [fixed]	0.02	0.02	0.02	0.02
Absorption ($\text{pcfabs}_{(N_H)}$)	10^{22} cm^{-2}	$0.84^{+0.08}_{-0.07}$	$2.39^{+\infty}_{-\infty}$	$0.69^{+0.08}_{-0.23}$	$0.004^{+\infty}_{-\infty}$
Covering fraction ($\text{pcfabs}_{(f_{cov})}$)		$0.95^{+0.007}_{-0.007}$	$0.73^{+0.14}_{-0.73}$	$0.98^{+\infty}_{-0.07}$	$0.01^{+\infty}_{-\infty}$
kT_{nei}	keV	$0.23^{+0.006}_{-0.006}$	$0.60^{+0.10}_{-0.09}$	$0.21^{+0.061}_{-0.008}$	$0.26^{+0.08}_{-0.01}$
Ionization timescale (τ)	$10^{10} \text{ s cm}^{-3}$	$10.37^{+6.00}_{-3.28}$	$18.03^{+\infty}_{-7.94}$	$5.83^{+\infty}_{-2.14}$	$0.005^{+\infty}_{-\infty}$
Normalization (nei)	10^{-4} cm^{-6}	$3.14^{+0.34}_{-0.32}$	$0.74^{+0.11}_{-0.10}$	$10.0^{+\infty}_{-1.77}$	$10.0^{+\infty}_{-2.03}$
Absorption ($\text{zxipcf}_{(N_H)}$)	10^{22} cm^{-2}	$62.22^{+0.64}_{-0.71}$	$64.65^{+11.51}_{-1.29}$	$60.49^{+1.13}_{-1.30}$	$61.47^{+1.34}_{-1.63}$
Ionization parameter $\log(\xi)$	erg cm s^{-1}	$1.72^{+0.18}_{-0.15}$	$1.95^{+0.02}_{-0.01}$	$1.41^{+0.17}_{-0.14}$	$1.37^{+0.24}_{-0.17}$
Covering fraction ($\text{zxipcf}_{f_{cov}}$)		$0.99^{+0.0003}_{-0.0004}$	$0.99^{+0.001}_{-0.001}$	$0.99^{+0.0005}_{-0.0006}$	$0.99^{+0.0006}_{-0.0008}$
kT_{nei}	keV	$10.99^{+1.74}_{-1.05}$	$10.79^{+2.43}_{-1.89}$	$16.0^{+\infty}_{-3.01}$	$7.06^{+1.25}_{-0.91}$
Ionization timescale (τ)	$10^{12} \text{ s cm}^{-3}$	$9.59^{+\infty}_{-8.19}$	$0.69^{+0.33}_{-0.19}$	$0.46^{+0.10}_{-0.08}$	$9.99^{+\infty}_{-9.05}$
Normalization (nei)	10^{-3} cm^{-5}	$6.79^{+0.26}_{-0.25}$	$6.60^{+0.34}_{-0.33}$	$7.33^{+0.36}_{-0.34}$	$4.10^{+0.29}_{-0.27}$
Gauss (E_{line})	keV	$6.43^{+0.02}_{-0.02}$	$6.40^{+0.02}_{-0.01}$	$6.40^{+0.01}_{-0.01}$	$6.38^{+0.02}_{-0.02}$
Sigma (Gauss_{σ})	keV	$0.15^{+0.02}_{-0.02}$	$0.08^{+0.02}_{-0.02}$	$0.08^{+0.02}_{-0.01}$	$0.09^{+0.03}_{-0.03}$
Normalization (Gauss)	$10^{-5} \text{ ph cm}^{-2} \text{ s}^{-1}$	$10.04^{+0.99}_{-0.96}$	$8.72^{+1.33}_{-1.24}$	$10.36^{+1.31}_{-1.24}$	$5.78^{+0.93}_{-0.86}$
Unabsorbed Source Flux $F_{(0.3-8.0)\text{keV}}$	$10^{-12} \text{ erg cm}^{-2} \text{ s}^{-1}$	$1.51^{+2.46}_{-1.60}$	$1.82^{+0.20}_{-0.41}$	$1.66^{+0.54}_{-0.58}$	$0.86^{+0.26}_{-0.68}$
Luminosity $L_{(0.3-8.0)\text{keV}}$	$10^{30} \text{ erg s}^{-1}$	$8.76^{+14.21}_{-0.92}$	$10.52^{+10.36}_{-2.36}$	$9.59^{+3.12}_{-3.38}$	$5.00^{+1.52}_{-3.97}$
Cstat / dof		1.08/(117)	1.11/(60)	1.52/(58)	1.23/(28)

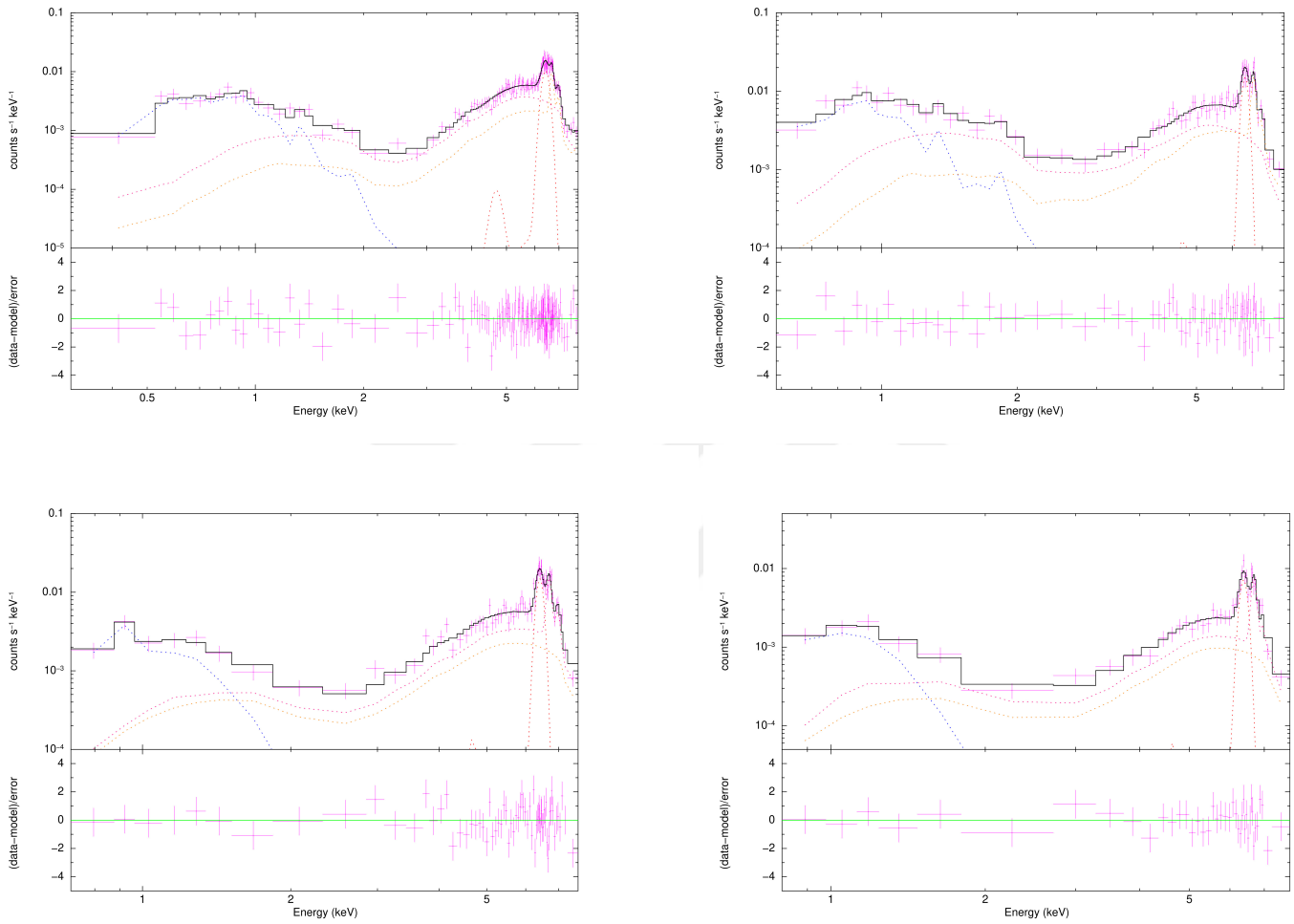


Figure 3.9: X-ray spectra and best-fit models of the $1''.5$ region around R Aqr using Model2 in 2017, 2020 (top panel, left to right), and 2021, 2022 (bottom panel, left to right). Data are shown in pink and fits are shown in black. The soft component is in blue, and the first emission component of the hard X-ray is in orange second is in vibrant pink. The Gauss line is shown in red dashed lines. The second panel of each spectrum shows the residuals of the fits in standard deviations.

Table 3.3: Spectral Fit Parameters in the 1".5 central source region.Model2 is used: $\text{tbabs} \times (\text{pcfabs} \times \text{nei} + \text{zxipcf} \times (\text{bremss} + \text{nei} + \text{gauss}))$

Quantity	Unit	2017	2020	2021	2022
Interstellar Absorption (N_H)	10^{22} cm^{-2} [fixed]	0.02	0.02	0.02	0.02
Absorption ($\text{pcfabs}_{(N_H)}$)	10^{22} cm^{-2}	$0.74^{+0.32}_{-0.26}$	$0.13^{+0.11}_{-0.11}$	$0.82^{+0.34}_{-0.25}$	$0.93^{+1.49}_{-0.42}$
Covering fraction ($\text{pcfabs}_{(f_{cov})}$)		$0.85^{+0.04}_{-0.09}$	$1.0^{+\infty}_{-0.71}$	$0.99^{+\infty}_{-0.03}$	$0.98^{+\infty}_{-0.07}$
kT_{nei}	keV	$0.39^{+0.05}_{-0.03}$	$0.90^{+0.69}_{-0.30}$	$0.16^{+0.05}_{-0.04}$	$0.11^{+0.02}_{-0.02}$
Ionization timescale (τ)	$10^{10} \text{ s cm}^{-3}$	$20.59^{+8.10}_{-4.85}$	$12.39^{+19.69}_{-5.47}$	$3.76^{+3.45}_{-1.57}$	$0.21^{+4.15}_{-\infty}$
Normalization (nei)	10^{-5} cm^{-6}	$4.43^{+0.50}_{-0.47}$	$1.69^{+0.27}_{-0.25}$	$2653.86^{+547.38}_{-495.07}$	$51374.4^{+13243.9}_{-11727.0}$
Absorption ($\text{zxipcf}_{(N_H)}$)	10^{22} cm^{-2}	$60.57^{+0.76}_{-0.89}$	$62.15^{+0.99}_{-1.18}$	$59.66^{+1.30}_{-1.58}$	$61.23^{+1.38}_{-1.77}$
Ionization parameter $\log(\xi)$	erg cm s^{-1}	$1.09^{+0.06}_{-0.18}$	$1.32^{+0.13}_{-0.10}$	$1.12^{+0.12}_{-0.20}$	$1.10^{+0.15}_{-0.27}$
Covering fraction ($\text{zxipcf}_{(f_{cov})}$)		$0.99^{+0.0001}_{-0.0001}$	$0.99^{+0.0005}_{-0.0006}$	$0.99^{+0.0004}_{-0.0004}$	$0.99^{+0.0004}_{-0.0005}$
kT_{bremss}	keV	$4.49^{+1.33}_{-0.87}$	$3.20^{+0.88}_{-0.63}$	$9.99^{+\infty}_{-5.42}$	$6.50^{+\infty}_{-3.12}$
Normalization (bremss)	10^{-3} cm^{-5}	$5.07^{+0.58}_{-0.58}$	$6.32^{+0.96}_{-0.97}$	$1.64^{+0.49}_{-0.50}$	$1.04^{+0.38}_{-0.39}$
kT_{nei}	keV	$10.14^{+2.97}_{-2.22}$	$13.70^{+\infty}_{-4.91}$	$15.27^{+\infty}_{-4.29}$	$5.65^{+1.37}_{-1.29}$
Ionization timescale (τ)	$10^{11} \text{ s cm}^{-3}$	$5.60^{+2.87}_{-1.74}$	$3.13^{+1.15}_{-0.83}$	$3.61^{+1.06}_{-8.23}$	$94.33^{+\infty}_{-92.13}$
Normalization (nei)	10^{-3} cm^{-5}	$4.41^{+0.73}_{-0.70}$	$5.07^{+0.83}_{-0.78}$	$5.96^{+1.01}_{-0.95}$	$3.88^{+0.88}_{-0.81}$
Gauss (E_{line})	keV	$6.42^{+0.02}_{-0.02}$	$6.40^{+0.02}_{-0.01}$	$6.41^{+0.01}_{-0.01}$	$6.38^{+0.02}_{-0.02}$
Sigma (Gauss_{σ})	keV	$0.12^{+0.02}_{-0.02}$	$0.08^{+0.03}_{-0.02}$	$0.07^{+0.02}_{-0.02}$	$0.08^{+0.04}_{-0.03}$
Normalization (Gauss)	$10^{-5} \text{ ph cm}^{-2} \text{ s}^{-1}$	$11.75^{+1.32}_{-1.27}$	$10.82^{+1.77}_{-1.66}$	$11.26^{+1.56}_{-1.47}$	$6.19^{+1.07}_{-1.00}$
Unabsorbed Source Flux $F_{(0.3-8.0)keV}$	$10^{-12} \text{ erg cm}^{-2} \text{ s}^{-1}$	$1.51^{+0.02}_{-0.02}$	$1.79^{+0.05}_{-0.05}$	$2.17^{+0.08}_{-0.05}$	$1.43^{+0.08}_{-0.12}$
Luminosity $L_{(0.3-8.0)keV}$	$10^{30} \text{ erg s}^{-1}$	$8.76^{+0.14}_{-0.15}$	$10.38^{+0.32}_{-0.33}$	$12.53^{+0.51}_{-0.33}$	$8.28^{+0.49}_{-0.71}$
Cstat / dof		0.85/(115)	1.03/(58)	1.41/(56)	0.85/(26)

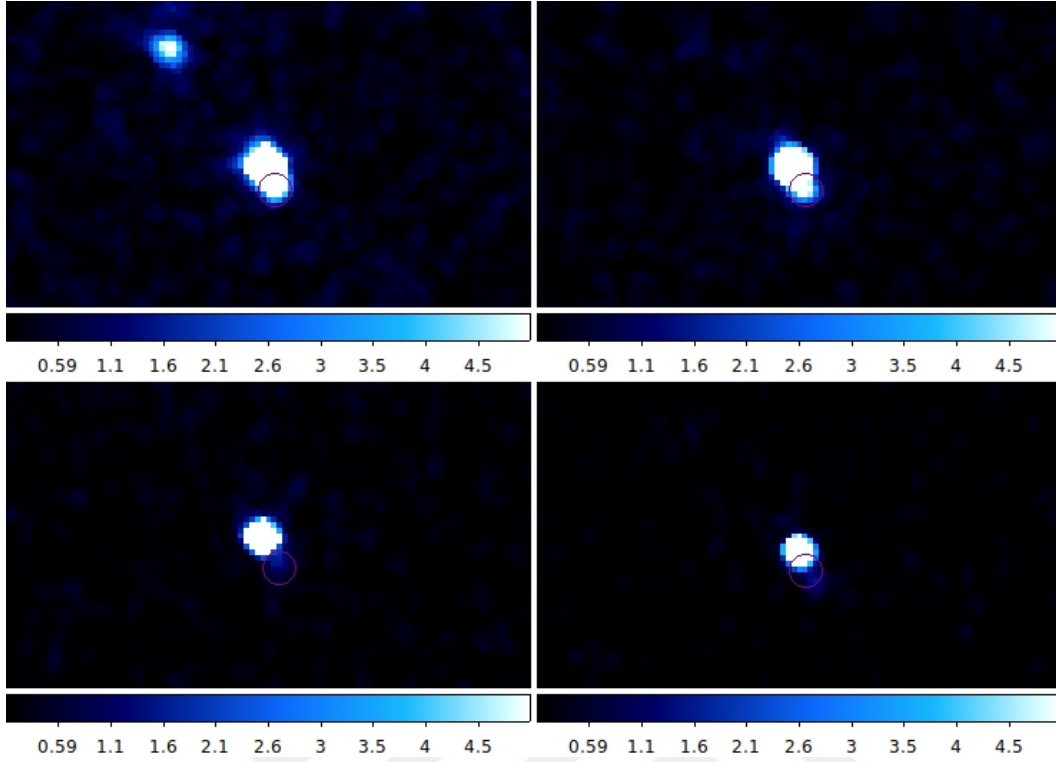


Figure 3.10: The 1.5'' circular regions from which the off-center spectra were chosen are indicated by the purple circles. The top left shows 2017 data the top right 2020 data, the bottom left 2021 data, and the bottom right is the 2022 data.

Table 3.4: Spectral Fit Parameters in the 1''.5 off-center region.
Model is used: $t\text{babs} \times (\text{pcfabs} \times \text{nei})$

Quantity	Unit	2017	2020	2021	2022
Interstellar Absorption (N_H)	10^{22} cm^{-2} [fixed]	0.02	0.02	0.02	0.02
Absorption ($\text{pcfabs}_{(N_H)}$)	10^{22} cm^{-2}	$61.22^{+7.03}_{-5.91}$	$4.13^{+1.90}_{-1.03}$	$9.79^{+\infty}_{-2.32}$	$36.17^{+\infty}_{-12.49}$
Covering fraction ($\text{pcfabs}_{(f_{cov})}$)		$0.99^{+0.00005}_{-0.00008}$	$0.97^{+0.009}_{-0.029}$	$0.99^{+0.001}_{-\infty}$	$0.99^{+0.001}_{-0.38}$
kT_{nei}	keV	$0.81^{+0.08}_{-0.07}$	$0.39^{+0.06}_{-0.05}$	$0.43^{+0.17}_{-0.11}$	$0.88^{+0.33}_{-0.29}$
Ionization timescale (τ)	10^9 s cm^{-3}	$7.42^{+1.61}_{-1.21}$	$46.13^{+51.03}_{-26.18}$	$8.97^{+13.19}_{-4.66}$	$10.85^{+36.91}_{-2.11}$
Normalization (nei)	10^{-4} cm^{-6}	$294.11^{+28.97}_{-27.71}$	$4.75^{+0.96}_{-0.87}$	$29.44^{+8.41}_{-7.48}$	$8.13^{+2.55}_{-2.11}$
Unabsorbed Source Flux $F_{(0.3-5.0)keV}$	$10^{-14} \text{ erg cm}^{-2} \text{ s}^{-1}$	$7.61^{+0.38}_{-0.46}$	$7.75^{+0.74}_{-0.85}$	$9.70^{+1.70}_{-1.39}$	$3.63^{+0.65}_{-0.75}$
Luminosity $L_{(0.3-5.0)keV}$	$10^{29} \text{ erg s}^{-1}$	$4.39^{+0.22}_{-0.26}$	$4.47^{+0.42}_{-0.04}$	$5.60^{+0.98}_{-0.80}$	$2.09^{+0.37}_{-0.43}$
Cstat / dof		0.88/(55)	0.86/(21)	0.99/(6)	1.12/(7)

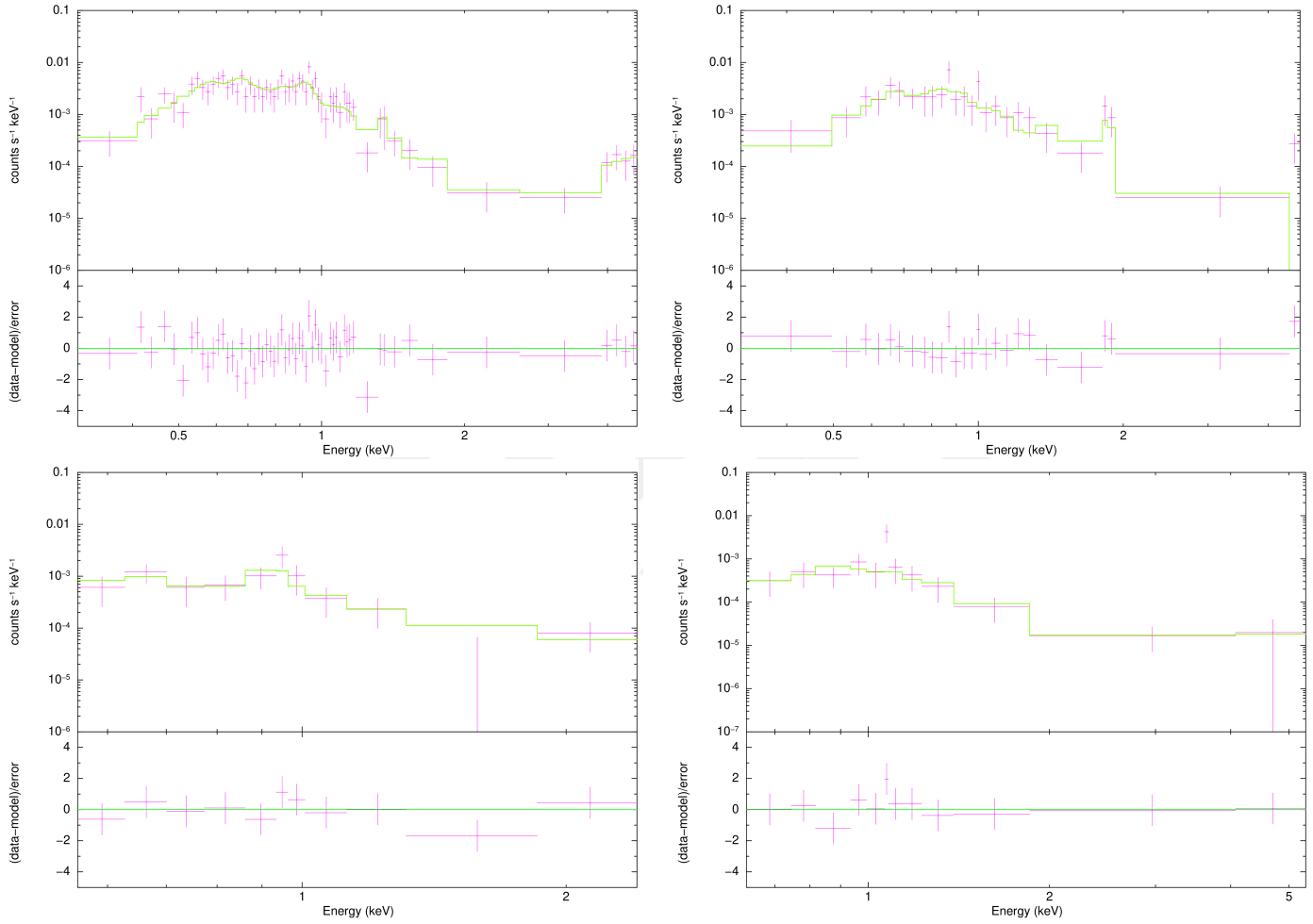


Figure 3.11: X-ray spectra of 1".5 region towards the SW direction of R Aqr in the years 2017, 2020 (top panel, left to right), and 2021, 2022 (bottom panel, left to right). Data are shown in pink and fits are shown in green. The second panel of each spectrum shows the residuals of the fits in standard deviations.

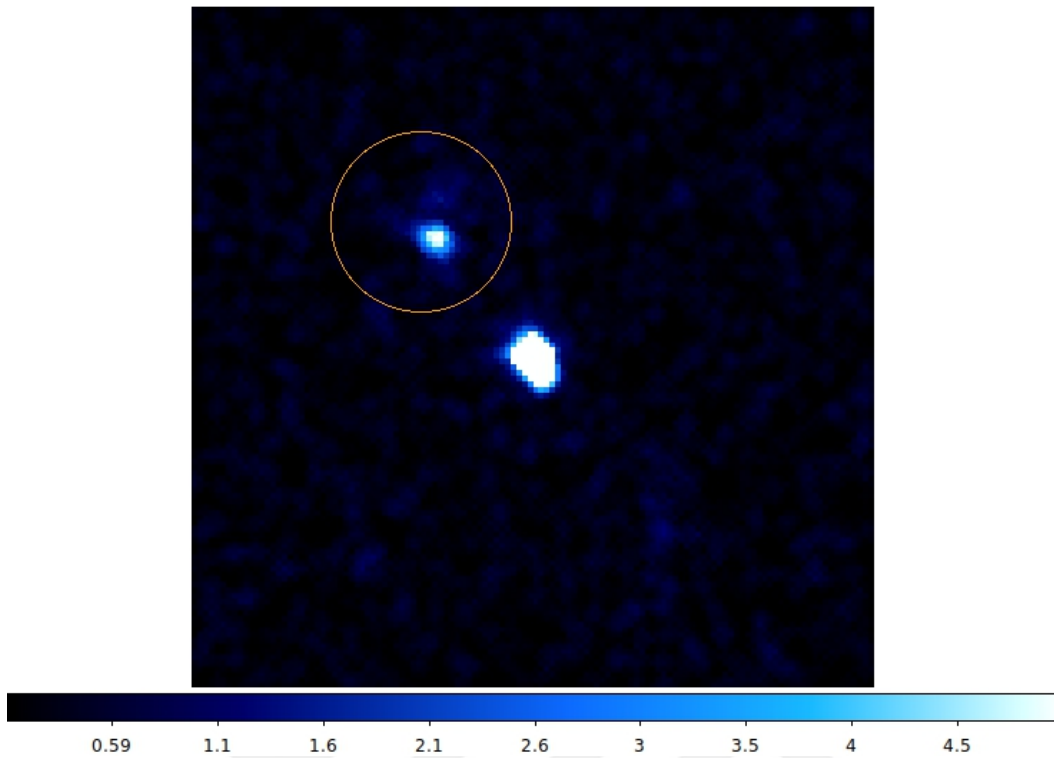


Figure 3.12: The yellow circle shows the 8'' radius region from which the NE spectrum of 2017 was extracted.

3.3.3. Spectrum of 8'' Region Towards to NE Direction

In the northeast region of the 2017 data, there was an old jet remnant, located $\approx 7''$ away from the central source of R Aqr. However, this structure was not detected in subsequent observations for approximately two years i.e. 2020, 2021, and 2022. As a result, this structure is analyzed for one data set.

The NE spectrum was obtained from two observations that were made in 2017, by selecting the same regions that are shown in Figure 3.12. These two spectra were combined with the *combine_spectra* task. The combined spectrum was binned with 7 counts/bin using the *dmgroup* task with *groupype=NUM_CTS* option. The spectrum was analyzed in the range of 0.3 - 3.0 keV. This energy range was selected below 3.0 keV due to the low count statistic. Since only the soft part of the spectrum was analyzed, the model used for the off-center spectrum is also used for this spectrum i.e. "tbabs \times (pcfabs \times nei)". Figure 3.13 shows the X-ray spectrum for the NE region and the best fits. The spectral parameters are outlined in Table 3.5.

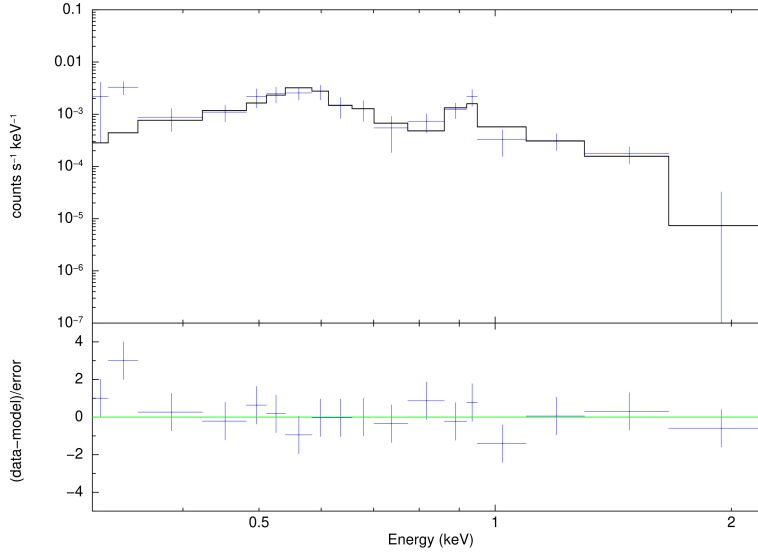


Figure 3.13: X-ray spectrum of 8'' region in the NE direction of R Aqr in the year 2017. Data are shown in blue and fits are shown in black. The lower panel shows the residuals of the fit in standard deviations.

Table 3.5: Spectral Fit Parameters of the 8'' radius region in the NE direction. Model is used: $t\text{babs} \times (\text{pcfabs} \times \text{nei})$

Quantity	Unit	2017.7
Interstellar Absorption (N_H)	10^{22} cm^{-2} [fixed]	0.02
Absorption ($\text{pcfabs}_{(N_H)}$)	10^{22} cm^{-2}	$1.10^{+0.23}_{-0.19}$
Covering fraction ($\text{pcfabs}_{(f_{cov})}$)		$0.98^{+0.006}_{-0.010}$
kT_{nei}	keV	$0.14^{+0.01}_{-0.01}$
Ionization timescale (τ)	$10^{11} \text{ s cm}^{-3}$	$1.38^{+1.75}_{-0.75}$
Normalization (nei)	10^{-3} cm^{-6}	$2.44^{+0.40}_{-0.37}$
Unabsorbed Source Flux $F_{(0.3-3.0)keV}$	$10^{-14} \text{ erg cm}^{-2} \text{ s}^{-1}$	$6.41^{+0.68}_{-0.59}$
Luminosity $L_{(0.3-3.0)keV}$	$10^{29} \text{ erg s}^{-1}$	$3.70^{+0.34}_{-0.39}$
Cstat / dof		1.51/(13)

4. DISCUSSIONS AND CONCLUSIONS

In this section, we present a detailed discussion on the morphological variations of R Aqr . It also contains a comprehensive description of the spectral analysis for three regions, namely the central region, the off-center region, and the NE region. In addition, spectral parameters are described in detail.

4.1. X-RAY MORPHOLOGY OF R AQR

We present multi-epoch X-ray images of R Aqr in Figures 3.2, 3.3, 3.4, and 3.5. While Figure 3.2 shows broad band (0.3-10.0 keV) X-ray images, the other figures show particular energy range images.

It is well known that R Aqr has a bipolar jet structure that extends from the central region to the northeast and southwest directions. Despite previous indications of the presence of jet structures, in the most recent observations carried out with the Chandra telescope, we did not observe these bipolar outflows.

In the examination of the 2017 data, an old jet remnant was discovered in the northeast region of the soft X-ray images. The remnant is clearly visible in the Figure 3.6 narrow band image revealing the interaction zone (with circus in art environment) of a previously active jet.

Our findings suggest that the detected jet remnant is most likely the same NE jet referred to in Melnikov's 2018 article. This is based on the fact that the position of the NE jet in the HST images obtained in 2014 as mentioned in the article coincides with the position of the detected jet remnant in 2017. In subsequent Chandra observations, the remnant is not detected. This suggests that the remnant cooled down and ultimately disappeared.

In all epochs, we did not observe any indications of an old jet structure in the SW direction. The extended region around the central source observed in the soft X-ray images between 2017 and 2022 appears to be directed toward the SW. Although this orientation was initially thought to be a new jet interaction directed towards the SW direction, this structure has

gradually disappeared over all epochs, especially after the 2021 epoch. Therefore, this hypothesis may not be reliable because if there was a new jet interaction we anticipate that increase or permanence in X-ray emissions. Also, the spectra of these regions showed this fading between 2017 and 2022.

Our analysis suggest that mid-band X-ray images are a point-like in the central region, whereas hard-band X-ray images reveal a more extended structure.

4.2. X-RAY SPECTRA OF R AQR

4.2.1. Central Region Spectra Using Model1

Utilizing two absorption models, i.e. *pcfabs* (partial covering by neutral absorber) and *zxipcf* (partial covering by ionized absorber), two distinct absorption features were observed in the spectra of the central region in the soft and hard X-ray bands.

The partial covering of the neutral absorber model contains two parameters; the first parameter is the hydrogen column density N_H and the second is the covering fraction of the material. The covering fraction is dimensionless and is $0 < f_{cov} \leq 1$.

In the 2017 fits (Table 3.2), the partial covering cold absorption for the soft X-ray component was found to be $N_H \approx 0.84 \times 10^{22} \text{ cm}^{-2}$. This was followed by a sudden increase of $N_H \approx 2.39 \times 10^{22} \text{ cm}^{-2}$ in the year 2020, and then a decreasing trend was observed after 2020. In 2022, N_H drops by a factor of 200 compared to 2017, to $N_H \approx 0.004 \times 10^{22} \text{ cm}^{-2}$.

In a plasma, equilibrium is defined as the ionization rate is equal to the recombination rate. When the plasma is in thermodynamic equilibrium, the temperature of the plasma is uniform. On the other hand, non-equilibrium ionization in the plasma is defined as the ionization rate not being equal to the recombination rate. This instability in the plasma can occur due to rapid changes in temperature or density, or due to photo-ionization effects. The NEI (non-equilibrium ionization) model was employed to account for dynamic fluctuations in ionization states, simplifying complex plasma dynamics. The NEI model is characterized by a constant temperature and a single ionization timescale parameter.

In the soft part of the spectra, the plasma temperature was found to be $kT \approx 0.23$ keV in 2017. In 2020, this was followed by an increase of $kT \approx 0.60$ keV, then dropped to $kT \approx 0.21$ keV in the next observation. In 2022 it stayed around this value with $kT \approx 0.26$ keV. The temperature values with errors are presented in Table 3.2.

The ionization timescale is defined as $\tau = n_e t$ with the unit $[\text{s cm}^{-3}]$ where n_e is the electron density and t represents the time after explosion or collision.

The ionization timescale in the soft X-ray component of the spectra was around $\tau \approx 10^{11}$ s cm^{-3} in 2017 and 2020. It then dropped to $\tau \approx 10^{10}$ s cm^{-3} in 2021, followed by a sharp decrease with $\tau \approx 10^7$ s cm^{-3} in 2022.

The *zxcipcf* model has described by the parameters 1) the equivalent column density N_H , 2) covering fraction f_{cov} , 3) logarithm ionization parameter $\log(\xi)$.

The ionized absorption in the hard part of the spectra was found to be high with $N_H \approx 62.2 \times 10^{22}$ cm^{-2} in 2017. In the rest of the ionized absorption remained between $N_H \approx 60.5 - 64.7 \times 10^{22}$ cm^{-2} .

The ionization parameter determines the ionization level of the medium and it is defined as

$$\xi = \frac{L}{nr^2} \quad (4.1)$$

where L is the luminosity of the ionizing source, n is the density of the medium, and r is the distance from the ionizing source to the medium. The unit of the ionization parameter is erg cm s^{-1} . While a value of $\log(\xi) \leq 0$ indicates a neutral or low ionisation medium, $\log(\xi) \geq 2$ indicates highly ionized medium.

$\log(\xi)$, the logarithm of the ionization parameter, is found to be $\log(\xi) \approx 1.72_{-0.15}^{+0.18}$ erg cm s^{-1} in 2017. It increased in 2020 with the value of $\log(\xi) \approx 1.95_{-0.01}^{+0.02}$ erg cm s^{-1} . Then it showed a decreasing trend in 2021 and 2022 with $\log(\xi) \approx 1.41_{-0.14}^{+0.17}$ erg cm s^{-1} and $\log(\xi) \approx 1.37_{-0.17}^{+0.24}$ erg cm s^{-1} , respectively.

The plasma temperature of the hard component of the central region spectra was around $kT \approx 10\text{-}13$ keV between 2017-2021, it was observed to drop to $kT \approx 7$ keV in 2022. The corresponding shock velocities, calculated from (2.9), were $v \approx 2371$ km s⁻¹ in 2017 and $v \approx 2046$ km s⁻¹ in 2022.

In the hard X-ray component, ionization timescale was found on the order of $\tau \approx 10^{12}$ s cm⁻³ in 2017. Between 2020 and 2021 it decreased to $\tau \approx 10^{11}$ s cm⁻³, and in 2022 it increased back to $\tau \approx 10^{12}$ s cm⁻³. In general, equilibrium is reached in a medium at $\tau \approx 10^{13}$ s cm⁻³.

In the central region spectra, a peak was observed at the 6.4 keV Fe K α line. However, one Gaussian emission line model was insufficient in fitting the Fe complex lines. Consequently, another Gaussian model was added to Model1. This parameter was not fixed and did not exhibit any significant variation in the line center at $\sim 6.40_{-0.04}^{+0.05}$ keV across the epochs.

In the years 2017, 2020, and 2021, it was found that the unabsorbed source flux in the energy range of 0.3 to 8.0 keV had a value of approximately on the order of $F_{0.3-8.0keV} \approx 10^{-12}$ erg cm⁻² s⁻¹. However, after a rise $\approx 20\%$ in 2020 to $F_{0.3-8.0keV} \approx 1.82 \times 10^{-12}$ erg cm⁻² s⁻¹, the decline continued in subsequent observations. Moreover, there was a significant drop in the flux for 2022, where flux decreased by a factor of ten relative to the previous years. The corresponding luminosities are on the order of $L \approx 10^{30}$ erg s⁻² for the years 2017, 2021, 2022. In 2020, the source luminosity showed minor increase then decreased to about level in 2017.

4.2.2. Elaboration on the Central Region Spectra Using Model2

In our initial study, using Model1, we found that the plasma temperature in the hard X-rays was slightly higher than what was observed in previous papers. As a result, we derived Model2 to account for this second component in the hard X-ray and further investigate its potential impact on the plasma temperature and X-ray emissions.

Model2 was derived by incorporating the thermal bremsstrahlung component into the hard part of Model1. Thermal bremsstrahlung radiation, also known as braking radiation, is defined as the deceleration of a charged particle, such as an electron, by the electric field of other charged particles, such as protons or nuclei. This type of emission is typically observed in hot, diffuse astrophysical sources, such as galaxy clusters and supernova remnants (E.

Kellogg et.al., 1975). The bremsstrahlung model in XSPEC defines one plasma temperature parameter.

Although the parameters of Model2 and Model1 do not show the same values in both the soft and hard X-ray component of the spectrum, no significant difference was observed between the two models.

The partial covering cold absorption in the soft part of the spectra did not fluctuate as in Model 1. Similar values to the results of year 2017 were observed for all epochs and no significant changes were observed except for a sharp decrease from $N_H \approx 0.74 \times 10^{22} \text{ cm}^{-2}$ to $N_H \approx 0.13 \times 10^{22} \text{ cm}^{-2}$ in 2020. In Model1 partial covering cold absorption values for the years 2017 and 2020 were $N_H \approx 0.84 \times 10^{22} \text{ cm}^{-2}$ and $N_H \approx 2.39 \times 10^{22} \text{ cm}^{-2}$, respectively.

In 2017, the plasma temperature in the soft part was found to be approximately $kT \approx 0.39 \text{ keV}$. Over the next epochs, there were fluctuations in temperature, with an increase to $kT \approx 0.90 \text{ keV}$ in 2020, followed by a decrease to $kT \approx 0.16 \text{ keV}$ in 2021, and then a further decrease to $kT \approx 0.11 \text{ keV}$ in 2022.

Compared to Model1, the ionization timescale in the soft X-ray component is a factor of 10 less which is about $\tau \approx 10^{10} \text{ s cm}^{-3}$ for years 2017 and 2020. In 2021 it decreased further to $\tau \approx 10^9 \text{ s cm}^{-3}$ similar to the trend in Model1. In 2022 it decreased another further of to $\tau \approx 10^8 \text{ s cm}^{-3}$, which was a factor of 10 higher than for Model1.

We find that the ionized absorption in the hard X-ray component of the spectra is similar to Model1 and it remains constant between $N_H \approx (60.5 - 62.15) \times 10^{22} \text{ cm}^{-2}$.

The ionized warm absorber parameters are found to be slightly lower in Model2 than those found in Model1. It is observed in the range of $\log(\xi) \approx 1.09 - 1.32 \text{ erg cm s}^{-1}$.

The bremsstrahlung plasma temperature was found to be $kT \approx 4.5 \text{ keV}$ in 2017, decreasing to $kT \approx 3.2 \text{ keV}$ in 2020. In 2021 it showed an increase to $kT \approx 9.9 \text{ keV}$ but it dropped back in 2022 to $kT \approx 6.5 \text{ keV}$. However, the temperature values appear to be similar when considering the error bars.

Model2 analysis showed no significant variation in the plasma temperature of the NEI model. The temperature trend observed in Model1 was also consistent in Model2. The plasma temperature was approximately $\approx 10\text{-}15$ keV from 2017 to 2021, but it decreased to kT ≈ 5.7 keV in 2022.

The ionization timescale was found on the order of $\tau \approx 10^{11}$ between 2017 and 2020. It exhibited an increasing trend in 2022 by a factor of 10 ($\tau \approx 10^{12}$).

In contrast to Model1, the unabsorbed source flux did not decrease after 2020 but continued to increase in 2021 and then decreased in 2022 below the 2017 level. They are found to be on the order of $F_{(0.3-8.0)\text{keV}} \approx 10^{-12}$ erg cm $^{-2}$ s $^{-1}$ in all epochs. The corresponding luminosities are on the order of $L \approx 10^{30}$ erg s $^{-2}$ in 2017 and 2022. On the other hand, in 2020 and 2021 we find that this value of luminosity increase by a factor of ten.

4.2.3. On the Interpretation of the Off-center Region Spectra

After analyzing the off-center spectra, we discovered that the partial covering by the neutral absorber model differed significantly between 2017 and 2020 epochs.

In the years 2017 and 2022 plasma temperatures was found to be kT ≈ 0.81 keV and kT ≈ 0.88 keV, respectively. While the temperature values are close to each other corresponding column densities differ as $N_H \approx 61.2 \times 10^{22}$ cm $^{-2}$ in 2017 and $N_H \approx 36.2 \times 10^{22}$ cm $^{-2}$ in 2022. On the other hand, in 2020 and 2021, the plasma temperatures were close to each other with the values of kT ≈ 0.39 keV and kT ≈ 0.43 keV, respectively. The corresponding column densities were also found to be slightly close to each other as $N_H \approx 4.1_{-1.0}^{+1.9} \times 10^{22}$ cm $^{-2}$ and $N_H \approx 9.8_{-2.32}^{+\infty} \times 10^{22}$ cm $^{-2}$, respectively. The shock velocities were calculated from (2.9) as $v \approx 643$ km s $^{-1}$ in 2017 and $v \approx 446$ km s $^{-1}$ in 2020.

In 2017 and 2021 the ionization timescale was found to be on the order of $\tau \approx 10^9$ cm $^{-3}$ On the other hand in 2020 and 2022, it is found to be higher, on the order of $\tau \approx 10^{10}$ cm $^{-3}$.

In all epochs, it was found that the unabsorbed source flux between 0.3 - 5.0 keV was on the order of $F_{(0.3-5.0)\text{keV}} \approx 10^{-14}$ erg cm $^{-2}$ s $^{-1}$. Furthermore, this flux value exhibited slightly increasing trend from 2017 to 2021 but it dropped to $F_{0.3-5.0\text{keV}} \approx 3.6 \times 10^{-14}$ erg cm $^{-2}$ s $^{-1}$ in 2022. The corresponding luminosities are $L \approx 10^{29}$ erg s $^{-2}$ which are less than a factor of ten times compared to the central region luminosities in the same years.

4.2.4. NE Region Spectrum

The NE spectrum in 2017 within the energy range of 0.3 - 3.0 keV was analyzed using the same model as the off-center spectra. The results of the analysis showed that compared to the soft X-ray component of the central region spectrum of the 2017 data, the partial covering cold absorption was higher, with a value of $N_H \approx 1.10 \times 10^{22} \text{ cm}^{-2}$. Additionally, the plasma temperature was found to be lower than the soft X-ray component of the central region spectrum, with a value of $kT \approx 0.14 \text{ keV}$. Furthermore, the ionization timescale was found as $\tau \approx 1.38 \times 10^{11} \text{ s cm}^{-3}$ which is higher than the value found for the soft X-ray component of the central region spectrum by a factor of ten.

The unabsorbed source flux, with a value of $F_{(0.3-3.0)\text{keV}} \approx 6.41 \times 10^{-14} \text{ erg cm}^{-2} \text{ s}^{-1}$, was found to be close to the flux of the off-center spectrum in the year 2017. As expected the corresponding luminosity was of the same order, $L \approx 10^{29} \text{ erg s}^{-2}$, as the off-center spectrum in the year 2017.

4.3. COMPARISON WITH PREVIOUS CHANDRA OBSERVATIONS

In order to provide an accurate approach, it is necessary to conduct a comparison between the results of our analyses and the previous observational results. In previous X-ray papers, *Chandra* observation of R Aqr for the years 2000, 2003, and 2005 was analyzed. In the years 2000 and 2003 central region spectral temperature was $kT = 6.8 \text{ keV}$ as a frozen parameter, because 2000 data has fewer counts and lower statistics, it is calculated after 2004 data then frozen, and $kT = 6.8_{-2.4}^{+4.0} \text{ keV}$, respectively. Additionally, in the soft X-rays an extension to the SW direction was observed in 2003 observation compared to the previous one indicating a new jet activity in the SW direction. This activity was confirmed with simultaneous radio observations (Nichols et. al. 2007). In their 2018 HEAD conference poster, Nichols et al. analysed these three datasets, but the temperature parameters was not given. So, we analyzed the central region of 2005 data with using Model1. The resulting spectrum and the spectral parameters are presented in the appendix. We found $kT \approx 5.55 \text{ keV}$. The authors also noted that hard X-ray flux increased over these three epochs.

In all three dataset an outer jet located to NE direction was detected. The temperature values in the 0.2 - 1.0 keV energy range was found to $kT = 0.15_{-0.02}^{+0.02}$ and $kT = 0.14_{-0.02}^{+0.02}$ keV for the years 2000 and 2003. Subsequent data was analyzed in Toala et. el. 2022. The temperatures was found $kT = 0.09_{-0.03}^{+0.02}$ and $kT = 0.24_{-0.05}^{+0.09}$ for the 0.3 - 1.5 keV energy range. These two temperature values are consistent with our finding which is $kT = 0.14_{-0.01}^{+0.01}$ keV.

In these three datasets, 2000, 2003, 2005, the SW outer jet was also observed, but in our analyses of the recent *Chandra* data we did not detect any outer structure at the location of the SW direction.

During the eclipse Mira is covered by the accretion disk. In periastron passage contraction of the WD Roche-lobe cause the disruption outer parts of accretion disk. Perhaps some degree of variation in X-ray emission compared to 2000-2005 data can be expected.

In morphological view, two other jets were detected in the NE direction extending out to $\sim 8''$ from the binary in 2000, and in the SW direction extending out to $\sim 26''$ from the binary in 2000. In our analyses we detect just an outer jet directed to NE $\sim 8''$ from the central binary. Additionally, our analysis showed an extension to the SW $\sim 2''$ in central region, as had been seen in the previous datasets.

4.4. CONCLUSIONS

The observations were selected for imaging depending on the longest exposure time among those from the same year. Selected four data sets with the years and selected observations were 2017-19015, 2020-23108, 2021-24341, and 2022-27333. Three different energy band images were calculated from the event files employing the same procedures to provide identical images. These energy bands cover as 0.3 - 1.5 keV, 2.0 - 5.0 keV, and 5.0 - 8.0 keV.

The soft X-ray images showed a diffuse structure on the central region and this structure extends up to $\sim 2''$ through the SW direction. Moreover, the soft X-ray image in 2017 indicate an outer jet located in NE direction $\sim 8''$ away from the central region. This outer jet probably cooled down and became undetectable in subsequent observations. Furthermore, narrow-band images in the 0.3–0.7 keV energy range demonstrated a gradual fading of both the central and off-center regions. Additionally, there was no emission detected in 2021 and

2022 within this narrow-band energy range. This gradual fading in the SW direction can be seen on the soft band images but in 2021 and 2022, contrary to the narrow-band images, emission was detected even if fading was observed in the 0.3- 1.5 keV images.

In all epochs, the system exhibits a point-like structure in the X-rays above 2.0 keV, with the bulk of the emission coming from the central region. Interestingly, in the images of the central region X-ray emissions do not appear to be centered on the source coordinates of R Aqr. In contrast to the 2021 emission, which appears centred on the source location, the 2022 X-ray emission, especially in hard X-ray image, was not found to be coming from the exact location of the central binary. This deviation towards the SW is seen in both soft and hard X-ray images. Even if deviation is also seen in 2017 and 2020, it is more prominent in 2022. This indicates origin in the nebulosity with motion. The soft X-ray flux in the off-center region declines by a factor of 2 in 2022 compared to 2017, but we do not find a significant change in the temperature which may indicate similar shock temperatures in the moving outflow. A comparison of the flux in 2022 with that in 2017, despite similar temperatures, indicates an expansion of the region.

In spectral analysis, two circular regions with a radius of 1".5 were selected. The first region is located at the central binary location in all epochs. The second region, which we prefer to call the off-center region, is selected to be near the diffuse structure from the central region location in the SW direction. These two regions were selected in such a way that they did not overlap. The spectra derived from different observation IDs were co-added using *combinespectra* task. This resulted in four spectra covering the years: 2017, 2020, 2021 and 2022.

The spectra from the central region were analyzed using two composite models, Model1 which is [$\text{tbabs} \times (\text{pcfabs} \times \text{nei} + (\text{zxipcf} \times (\text{nei} + \text{gauss})))$] and Model2 which is [$\text{tbabs} \times (\text{pcfabs} \times \text{nei} + \text{zxipcf} \times (\text{bremss} + \text{nei} + \text{gauss}))$]. In the analysis of central region spectra, we employed two different absorption models, and detected of two different absorption features for the soft and hard X-ray components. The partial covering absorption model was employed to the soft X-ray components. In 2017, partial covering absorption was found as $N_H \approx 0.84 \times 10^{22} \text{ cm}^{-2}$, and it shows a drastic drop by a factor of 200 in 2022. The partially covering ionized absorption model was employed to the hard X-ray components of the spectra. In all epochs we found the approximate ionized absorption nearly

constant between $N_H \approx 60.5 - 64.7 \times 10^{22} \text{ cm}^{-2}$. No significant differences were observed between the absorption parameters of Model1 and Model2.

Two different plasma models were used for the soft and hard X-ray components of the spectra. The plasma temperatures for the soft component were found in all epochs near $kT \approx 0.23 \text{ keV}$ except the rise in 2020 to $kT \approx 0.60$. In Model2, the temperature parameters exhibited fluctuations, although it can be taken that they were comparable to those observed in Model1. It was determined that the plasma temperature of the hard component in Model1 was $kT \approx 10.0\text{-}13.0 \text{ keV}$ between 2017-2021, and decreased to $kT \approx 7.0 \text{ keV}$ in 2022. The findings are consistent with those of Model2, and the drastic drop in 2022 was observed in both models.

The approximate central region luminosities in the range 0.3 - 8.0 keV were found to $L_x \approx 5.0 - 10.52 \times 10^{30} \text{ erg s}^{-2}$ in Model1 and $L_x \approx 8.28 - 12.53 \times 10^{30} \text{ erg s}^{-2}$ in Model2. In both models, a drop was observed in 2022 with the lowest value.

Off-center region spectra revealed substantial changes in the absorption over these epochs. The observed pattern display a decline between 2017 and 2020 from $N_H \approx 61.22 \times 10^{22} \text{ cm}^{-2}$ to $N_H \approx 4.13 \times 10^{22} \text{ cm}^{-2}$, then followed by a subsequent rise to $N_H \approx 9.8 \times 10^{22} \text{ cm}^{-2}$, and then again in 2022 its showed further rise to $N_H \approx 36.17 \times 10^{22} \text{ cm}^{-2}$. It was observed that the approximate temperatures for the off-center region spectra varied between $kT \approx 0.8 \text{ keV}$ and $kT \approx 0.4 \text{ keV}$ depending on the N_H variation. The X-ray luminosities of the off-center were found as $L_x \approx 2.0 - 5.6 \times 10^{29} \text{ erg s}^{-2}$ in the range 0.3 - 5.0 keV. While the luminosity values observed in previous epochs, (2017-2020-2021), were relatively consistent, a notable decline was observed in 2022.

The approximate temperature in NE region spectrum was found as $kT \approx 0.14 \text{ keV}$. This value is consistent with the NE region temperatures found in 2001 and 2003. The X-ray luminosity of the NE region was found as $L_x \approx 3.7 \times 10^{29} \text{ erg s}^{-2}$ in the range 0.3 - 3.0 keV.

Despite all the works accumulated over the years, we believe that R Aqr remains a subject worthy of further investigation. The future observations of R Aqr with *Chandra*, which offers a unique spatial resolution, will provide a more detailed understanding of the origins of the morphological changes observed in the system. Observations with next-generation

high-energy missions such as ATHENA or XRISM will provide a deeper understanding of the dynamics of the system, such as the formation of jets. Additionally, obtaining simultaneous multi-wavelength observations will enable a comprehensive interpretation of the system.



REFERENCES

- Abate, C., Pols, O. R., Izzard, R. G., Mohamed, S. S., de Mink, S. E. 2013. Wind Roche-lobe overflow: Application to carbon-enhanced metal-poor stars. *Astronomy and Astrophysics* 552. doi:10.1051/0004-6361/201220007
- Akras, S., Guzman-Ramirez, L., Leal-Ferreira, M. L., Ramos-Larios, G. 2019. A Census of Symbiotic Stars in the 2MASS, WISE, and Gaia Surveys. *The Astrophysical Journal Supplement Series* 240. doi:10.3847/1538-4365/aaf88c
- Balman, Ş. 2020. Accretion flows in nonmagnetic white dwarf binaries as observed in X-rays. *Advances in Space Research* 66, 1097–1122. doi:10.1016/j.asr.2020.05.031
- Böhringer, H. 1998. Equilibrium Ionization and Non-Equilibrium Ionization Plasma Models. *IAU Colloq. 166: The Local Bubble and Beyond* 341–352. doi:10.1007/BFb0104745
- Borkowski, K. J. 2000. Nonequilibrium Ionization Models for Analysis of X-Ray Spectra of Supernova Remnants. *Revista Mexicana de Astronomia y Astrofisica Conference Series* 9, 288–289.
- Bozzo, E., Romano, P., Ferrigno, C., Ducci, L. 2024. Swift, NuSTAR, and INTEGRAL observations of the symbiotic X-ray binary IGR J16194-2810. *Monthly Notices of the Royal Astronomical Society* 527, 3585–3591. doi:10.1093/mnras/stad3509
- Cannon, A. J., Pickering, E. C. 1914. Stars Having Peculiar Spectra. *Harvard College Observatory Circular* 184.
- Cariková, Z., Skopal, A. 2012. Ionization structure of hot components in symbiotic binaries during active phases. *Astronomy and Astrophysics* 548. doi:10.1051/0004-6361/201219221
- Chen, X., Liu, Z., Han, Z. 2024. Binary stars in the new millennium. *Progress in Particle and Nuclear Physics* 134. doi:10.1016/j.pnpnp.2023.104083
- Coleman, M. S. B., Rafikov, R. R., Philippov, A. A. 2022. Boundary layers of accretion discs: Discovery of vortex-driven modes and other waves. *Monthly Notices of the Royal Astronomical Society* 509, 440–462. doi:10.1093/mnras/stab2962
- Contini, M. 1995. Shocks in Novae and in Symbiotic Stars. *Cataclysmic Variables* 205, 277. doi:10.1007/978-94-011-0335-0_84
- de Gouveia Dal Pino, E. M. 2005. Astrophysical jets and outflows. *Advances in Space Research* 35, 908–924. doi:10.1016/j.asr.2005.03.145
- Eze, R. N. C. 2014. Fe K α line in hard X-ray emitting symbiotic stars. *Monthly Notices of the Royal Astronomical Society* 437, 857–861. doi:10.1093/mnras/stt1947

- Girard, T., Willson, L. A. 1987. Winds in collision. III. Modeling the interaction nebulae of eruptivesymbiotics.. *Astronomy and Astrophysics* 183, 247–256.
- Gromadzki, M., Mikołajewska, J. 2009. The spectroscopic orbit and the geometry of R Aquarii. *Astronomy and Astrophysics* 495, 931–936. doi:10.1051/0004-6361:200810052
- Höfner, S., Freytag, B. 2022. Explaining the winds of AGB stars: Recent progress. *The Origin of Outflows in Evolved Stars* 366, 165–172. doi:10.1017/S1743921322000199
- Höfner, S., Olofsson, H. 2018. Mass loss of stars on the asymptotic giant branch. Mechanisms, models and measurements. *Astronomy and Astrophysics Review* 26. doi:10.1007/s00159-017-0106-5
- Kaastra, J. S. 2017. On the use of C-stat in testing models for X-ray spectra. *Astronomy and Astrophysics* 605. doi:10.1051/0004-6361/201629319
- Kallman, T., Dorodnitsyn, A. 2019. Warm Absorber Diagnostics of AGN Dynamics. *The Astrophysical Journal* 884. doi:10.3847/1538-4357/ab40aa
- Kellogg, E., Pedelty, J. A., Lyon, R. G. 2001. The X-Ray System R Aquarii: A Two-sided Jet and Central Source. *The Astrophysical Journal* 563, L151–L155. doi:10.1086/338594
- Kellogg, E. and 7 colleagues 2007. Outer Jet X-Ray and Radio Emission in R Aquarii: 1999.8 to 2004.0. *The Astrophysical Journal* 664, 1079–1087. doi:10.1086/518877
- Kenny, H. T., Taylor, A. R. 2005. Colliding Winds in Symbiotic Binary Systems. I. Analytic and Numerical Solutions. *The Astrophysical Journal* 619, 527–537. doi:10.1086/426309
- Kenyon, S. J., Webbink, R. F. 1984. The nature of symbiotic stars.. *The Astrophysical Journal* 279, 252–283. doi:10.1086/161888
- Lampland, C.O.: 1922, *Publications of the American Astronomical Society* 4, 319.
- Lee, Y.-M., Kim, H., Lee, H.-W. 2022. Formation of the Asymmetric Accretion Disk from Stellar Wind Accretion in an S-type Symbiotic Star. *The Astrophysical Journal* 931. doi:10.3847/1538-4357/ac67d6
- Leedjäv, L. 2014. Cataclysmic variables and symbiotic stars — challenging targets for small telescopes. *Contributions of the Astronomical Observatory Skalnaté Pleso* 43, 282–289.
- Livio, M. 2004. Astrophysical Jets. *Baltic Astronomy* 13, 273–279.
- Lopez-Coto, R. 2015. Very-high-energy gamma-ray observations of pulsar wind nebulae and cataclysmic variable stars with MAGIC and development of trigger systems for IACTs. Ph.D. Thesis.
- Luna, G. J. M., Sokoloski, J. L., Mukai, K., Nelson, T. 2013. Symbiotic stars in X-rays. *Astronomy and Astrophysics* 559. doi:10.1051/0004-6361/201220792

- Luna, G. J. M., Sokoloski, J. L., Mukai, K., Nelson, T., Nuñez, N. E. 2014. Symbiotic stars in X-rays and UV. *Revista Mexicana de Astronomía y Astrofísica Conference Series* 44, 158–159.
- Melnikov, S., Stute, M., Eisloffel, J. 2018. The bipolar jet of the symbiotic star R Aquarii: A study of its morphology using the high-resolution HST WFC3/UVIS camera. *Astronomy and Astrophysics* 612. doi:10.1051/0004-6361/201731749
- Merc, J. 2022. Multi-frequency research of symbiotic binaries. Ph.D. Thesis.
- Merrill, P. W., Humason, M. L. 1932. A Bright Line of Ionized Helium, $\lambda 4686$, in Three Stellar Spectra with Titanium Bands. *Publications of the Astronomical Society of the Pacific* 44, 56. doi:10.1086/124191
- Merrill, P. W. 1958. 51. Symbiosis in Astronomy: Introductory Report. *Liege International Astrophysical Colloquia* 8, 436–448.
- Mohamed, S., Podsiadlowski, P. 2007. Wind Roche-Lobe Overflow: a New Mass-Transfer Mode for Wide Binaries. *15th European Workshop on White Dwarfs* 372, 397.
- Muerset, U., Wolff, B., Jordan, S. 1997. X-ray properties of symbiotic stars. II. Systems with colliding winds.. *Astronomy and Astrophysics* 319, 201–210.
- Munari, U. 2019. The Symbiotic Stars. arXiv e-prints. doi:10.48550/arXiv.1909.01389
- Narayan, R., Popham, R. 1994. Accretion disk boundary layers. *Theory of Accretion Disks* - 2 417, 293.
- Navarro, S. G., Corral, L. J. 2013. Jets in Symbiotic Stars: The R Aqr Case. *Fluid Dynamics in Physics* 159–167. doi:10.1007/978-3-642-27723-8_10
- Nichols, J. S., DePasquale, J., Kellogg, E., Anderson, C. S., Sokoloski, J., Pedelty, J. 2007. Discovery of Rapid Hard X-Ray Variability and New Jet Activity in the Symbiotic Binary R Aquarii. *The Astrophysical Journal* 660, 651–661. doi:10.1086/512138
- No author 1935. Fig. 2. Analysis of light-curve of R Aquarii.. *Contributions from the Mount Wilson Observatory / Carnegie Institution of Washington* 513, 18–18.
- Perko, M. 2024. Accreting-only symbiotic stars in the era of large Galactic Archeology spectroscopic surveys. *Contributions of the Astronomical Observatory Skalnaté Pleso* 54, 75–84. doi:10.31577/caosp.2024.54.2.75
- Pickering, E. C. 1912. The Variable Star, 87.1911.. *Harvard College Observatory Circular* 176.
- Ricci, C., Beckmann, V., Audard, M., Courvoisier, T. J.-L. 2010. Multi-zone warm and cold clumpy absorbers in three Seyfert galaxies. *Astronomy and Astrophysics* 518. doi:10.1051/0004-6361/200912509
- Schmid, H. M. and 42 colleagues 2017. SPHERE/ZIMPOL observations of the symbiotic system R Aquarii. I. Imaging of the stellar binary and the innermost jet clouds. *Astronomy and Astrophysics* 602. doi:10.1051/0004-6361/201629416

- Smith, R. K., Hughes, J. P. 2010. Ionization Equilibrium Timescales in Collisional Plasmas. *The Astrophysical Journal* 718, 583–585. doi:10.1088/0004-637X/718/1/583
- Soker, N., Lasota, J.-P. 2004. The absence of jets in cataclysmic variable stars. *Astronomy and Astrophysics* 422, 1039–1043. doi:10.1051/0004-6361:20040402
- Soker, N., Regev, O. 2003. Launching jets from the boundary layer of accretion disks in young stellar objects. *Astronomy and Astrophysics* 406, 603–611. doi:10.1051/0004-6361:20030809
- Sokoloski, J. L., Bildsten, L. 2010. Evidence for the White Dwarf Nature of Mira B. *The Astrophysical Journal* 723, 1188–1194. doi:10.1088/0004-637X/723/2/1188
- Sopka, R. J., Herbig, G., Kafatos, M., Michalitsianos, A. G. 1982. Radio optical observations of the R AQR jet.. *The Astrophysical Journal* 258, L35–L39. doi:10.1086/183825
- Skopal, A. and 6 colleagues 2012. Recent photometry of symbiotic stars. *Astronomische Nachrichten* 333, 242. doi:10.1002/asna.201111655
- Skopal, A. and 18 colleagues 2020. The path to Z And-type outbursts: The case of V426 Sagittae (HBHA 1704-05). *Astronomy and Astrophysics* 636. doi:10.1051/0004-6361/201937199
- Skopal, A. 2024. Exploring outbursts of accreting white dwarfs in symbiotic binaries - basic concept. *Contributions of the Astronomical Observatory Skalnaté Pleso* 54, 85–97. doi:10.31577/caosp.2024.54.2.85
- Starrfield, S., Iliadis, C., Hix, W. R. 2016. The Thermonuclear Runaway and the Classical Nova Outburst. *Publications of the Astronomical Society of the Pacific* 128, 051001. doi:10.1088/1538-3873/128/963/051001
- Stute, M., Camenzind, M. 2005. Are jets in symbiotic stars driven by magnetic fields?. *Astronomy and Astrophysics* 432, L17–L20. doi:10.1051/0004-6361:200500012
- Toalá, J. A. 2024. Reflection physics in X-ray-emitting symbiotic stars. *Monthly Notices of the Royal Astronomical Society* 528, 987–996. doi:10.1093/mnras/stae039
- Tosi, S., Dell’Agli, F., Huerta-Martinez, E., Ventura, P. 2022. Dust Formation in the Wind of AGB Stars—The Effects of Mass, Metallicity and Gas-Dust Drift. *Universe* 8. doi:10.3390/universe8050270
- Willson, L. A., Garnavich, P., Mattei, J. A. 1981. 1978 Eclipse of R Aquarii. *Information Bulletin on Variable Stars* 1961, 1.
- Yang, H.-J., Park, M.-G., Cho, S.-H., Park, C. 2005. Korean nova records in A.D. 1073 and A.D. 1074: R Aquarii. *Astronomy and Astrophysics* 435, 207–214. doi:10.1051/0004-6361:20042455

APPENDIX

1. 2005 Chandra Data

Chandra archival data obtained in 2005 was analyzed using Model1 which is "tbabs × (pcfabs × nei + (zxipcf × (nei + gauss)))". 1".5 circular region central at the binary coordinates was selected. Spectrum was extracted using *specextract* task. The derived spectrum was binned using *dmgroup* task with the *group_type = NUM_CTS* option with 5 counts/bin. The spectrum and the best fit are presented in Figure 1.1. The spectral parameters are shown in Table 1.1.

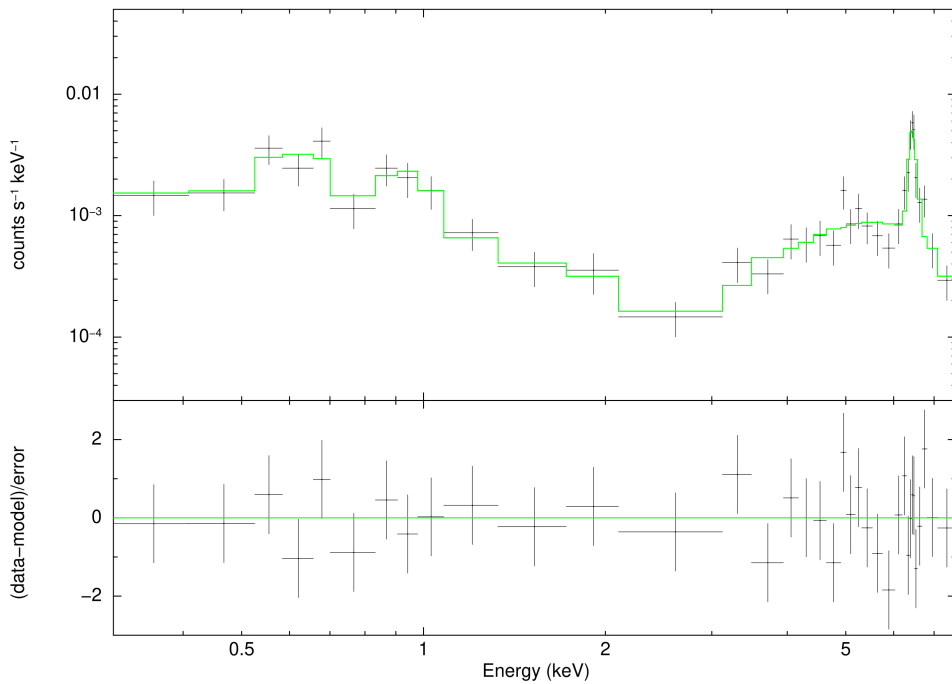


Figure 1.1: Chandra X-ray spectrum and the best fit model of 1".5 region around R Aqr using data obtained in 2005. Data are shown in black and fit is in green. The second panel of the spectrum shows the residuals of the fit in standard deviations.

Table 1.1: Spectral Parameters of the central region with a radius of 1".5 radius for the 2005 epoch.

Model is used: $\text{tbabs} \times ((\text{pcfabs} \times \text{nei}) + \text{zxipcf} \times (\text{nei} + \text{gauss}))$

Quantity	Unit	2005.7
Interstellar Absorption (N_H)	10^{22} cm^{-2} [fixed]	0.02
Absorption ($\text{pcfabs}_{(N_H)}$)	10^{22} cm^{-2}	$2.76^{+3.55}_{-1.27}$
Covering fraction ($\text{pcfabs}_{(f_{cov})}$)		$0.92^{+0.03}_{-0.13}$
kT_{nei}	keV	$1.32^{+0.82}_{-0.52}$
Ionization timescale (τ)	10^8 s cm^{-3}	$3.19^{+1.87}_{-1.02}$
Normalization (nei)	10^{-3} cm^{-5}	$3.37^{+0.93}_{-0.82}$
Absorption ($\text{zxipcf}_{(N_H)}$)	10^{22} cm^{-2}	$5.88^{+2.48}_{-3.42}$
Ionization parameter $\log(\xi)$	erg cm s^{-1}	$0.17^{+0.49}_{-\infty}$
Covering fraction ($\text{zxipcf}_{(f_{cov})}$)		$0.99^{+\infty}_{-0.00004}$
kT_{nei}	keV	$5.55^{+2.45}_{-1.23}$
Ionization timescale (τ)	$10^{10} \text{ s cm}^{-3}$	$2.33^{+0.61}_{-0.50}$
Normalization (nei)	10^{-3} cm^{-3}	$4.38^{+0.53}_{-0.52}$
Gauss (E_{line})	keV	$6.41^{+0.03}_{-0.02}$
Sigma ($Gauss_{\sigma}$)	keV	$0.0001^{+0.07}_{-\infty}$
Normalization ($Gauss$)	$10^{-5} \text{ ph cm}^{-2} \text{ s}^{-1}$	$3.11^{+1.14}_{-0.99}$
Unabsorbed Source Flux $F_{(0.3-8.0)keV}$	$10^{-13} \text{ erg cm}^{-2} \text{ s}^{-1}$	$3.10^{+0.15}_{-0.18}$
Luminosity $L_{(0.3-8.0)keV}$	$10^{30} \text{ erg s}^{-1}$	$1.79^{+0.09}_{-0.11}$
Cstat / dof		1.16/(22)



Curriculum Vitae

Personal Information	
Name Surname	Havva BOSTAN
Place of birth	
Date of birth	
Nationality	<input checked="" type="checkbox"/> T.C. <input type="checkbox"/> Other
E-mail	

Education	
Bachelor Degree	
University	Istanbul University
Department	Faculty of Science
Program	Astronomy and Space Science
Graduation Year	2020

Master Degree	
University	Istanbul University
Institute	Institute of Science
Department	Astronomy and Space Science
Program	Astronomy and Astrophysics
Graduation Year	2024

Article and Papers
<i>Articles</i>